Draft version July 4, 2025
Typeset using LaTeX **twocolumn** style in AASTeX63

The dark matter content of Milky Way dwarf spheroidal galaxies: Draco, Sextans and Ursa Minor

Hao Yang,[1,2,3] Wenting Wang,[1,3] Ling Zhu,[4] Ting S. Li,[5] Sergey E. Koposov,[6,7] Jiaxin Han,[1,3] Songting Li,[1,3] Rui Shi,[1,3] Monica Valluri,[8,9] Alexander H. Riley,[10] Arjun Dey,[11] Constance Rockosi,[12,13,14] Carles G. Palau,[1,3] Jessica Nicole Aguilar,[15] Steven Ahlen,[16] David Brooks,[17] Todd Claybaugh,[15] Andrew Cooper,[18] Axel de la Macorra,[19] Peter Doel,[17] Simone Ferraro,[15,20] Jaime E. Forero-Romero,[21,22] Enrique Gaztañaga,[23,24,25] Satya Gontcho A Gontcho,[15] Alma Xochitl Gonzalez Morales,[26] Gaston Gutierrez,[27] Julien Guy,[15] Klaus Honscheid,[28,29,30] Mustapha Ishak,[31] Dick Joyce,[11] Robert Kehoe,[32] Theodore Kisner,[15] Namitha Kizhuprakkat,[18,33] Anthony Kremin,[15] Ofer Lahav,[17] Martin Landriau,[15] Laurent Le Guillou,[34] Gustavo Medina Toledo,[35] Aaron Meisner,[11] Ramon Miquel,[36,37] Nathalie Palanque-Delabrouille,[38,15] Francisco Prada,[39] Ignasi Pérez-Ràfols,[40] Graziano Rossi,[41] Eusebio Sanchez,[42] David Schlegel,[15] Michael Schubnell,[43,9] Joseph Harry Silber,[15] David Sprayberry,[11] Gregory Tarlé,[9] Benjamin Alan Weaver,[11] Rongpu Zhou,[15] and Hu Zou[44]

[1] *Department of Astronomy, School of Physics and Astronomy, and Shanghai Key Laboratory for Particle Physics and Cosmology, Shanghai Jiao Tong University, Shanghai 200240, People's Republic of China*
[2] *Tsung-Dao Lee Institute, Shanghai Jiao Tong University, Shanghai, 201210, China*
[3] *State Key Laboratory of Dark Matter Physics, School of Physics and Astronomy,Shanghai Jiao Tong University, Shanghai 200240, China*
[4] *Shanghai Astronomical Observatory, Chinese Academy of Sciences, 80 Nandan Road, Shanghai 200030, China*
[5] *Department of Astronomy and Astrophysics, University of Toronto, 50 St. George Street, Toronto ON, M5S 3H4, Canada*
[6] *Institute for Astronomy, University of Edinburgh, Royal Observatory, Blackford Hill, Edinburgh EH9 3HJ, UK*
[7] *Institute of Astronomy, University of Cambridge, Madingley Road, Cambridge CB3 0HA, UK*
[8] *Department of Astronomy, University of Michigan, Ann Arbor, MI 48109, USA*
[9] *University of Michigan, 500 S. State Street, Ann Arbor, MI 48109, USA*
[10] *Institute for Computational Cosmology, Department of Physics, Durham University, South Road, Durham DH1 3LE, UK*
[11] *NSF NOIRLab, 950 N. Cherry Ave., Tucson, AZ 85719, USA*
[12] *Department of Astronomy and Astrophysics, UCO/Lick Observatory, University of California, 1156 High Street, Santa Cruz, CA 95064, USA*
[13] *Department of Astronomy and Astrophysics, University of California, Santa Cruz, 1156 High Street, Santa Cruz, CA 95065, USA*
[14] *University of California Observatories, 1156 High Street, Sana Cruz, CA 95065, USA*
[15] *Lawrence Berkeley National Laboratory, 1 Cyclotron Road, Berkeley, CA 94720, USA*
[16] *Department of Physics, Boston University, 590 Commonwealth Avenue, Boston, MA 02215 USA*
[17] *Department of Physics & Astronomy, University College London, Gower Street, London, WC1E 6BT, UK*
[18] *Institute of Astronomy and Department of Physics, National Tsing Hua University, 101 Kuang-Fu Rd. Sec. 2, Hsinchu 30013, Taiwan*
[19] *Instituto de Física, Universidad Nacional Autónoma de México, Circuito de la Investigación Científica, Ciudad Universitaria, Cd. de México C. P. 04510, México*
[20] *University of California, Berkeley, 110 Sproul Hall #5800 Berkeley, CA 94720, USA*
[21] *Departamento de Física, Universidad de los Andes, Cra. 1 No. 18A-10, Edificio Ip, CP 111711, Bogotá, Colombia*
[22] *Observatorio Astronómico, Universidad de los Andes, Cra. 1 No. 18A-10, Edificio H, CP 111711 Bogotá, Colombia*
[23] *Institut d'Estudis Espacials de Catalunya (IEEC), c/ Esteve Terradas 1, Edifici RDIT, Campus PMT-UPC, 08860 Castelldefels, Spain*
[24] *Institute of Cosmology and Gravitation, University of Portsmouth, Dennis Sciama Building, Portsmouth, PO1 3FX, UK*
[25] *Institute of Space Sciences, ICE-CSIC, Campus UAB, Carrer de Can Magrans s/n, 08913 Bellaterra, Barcelona, Spain*
[26] *Departamento de Física, DCI-Campus León, Universidad de Guanajuato, Loma del Bosque 103, León, Guanajuato C. P. 37150, México*
[27] *Fermi National Accelerator Laboratory, PO Box 500, Batavia, IL 60510, USA*
[28] *Center for Cosmology and AstroParticle Physics, The Ohio State University, 191 West Woodruff Avenue, Columbus, OH 43210, USA*
[29] *Department of Physics, The Ohio State University, 191 West Woodruff Avenue, Columbus, OH 43210, USA*
[30] *The Ohio State University, Columbus, 43210 OH, USA*
[31] *Department of Physics, The University of Texas at Dallas, 800 W. Campbell Rd., Richardson, TX 75080, USA*
[32] *Department of Physics, Southern Methodist University, 3215 Daniel Avenue, Dallas, TX 75275, USA*
[33] *Center for Informatics and Computation in Astronomy, NTHU, 101 Kuang-Fu Rd. Sec. 2, Hsinchu 30013, Taiwan*
[34] *Sorbonne Université, CNRS/IN2P3, Laboratoire de Physique Nucléaire et de Hautes Energies (LPNHE), FR-75005 Paris, France*

Corresponding author: Wenting Wang
wenting.wang@sjtu.edu.cn

[35] Department of Astronomy & Astrophysics, University of Toronto, Toronto, ON M5S 3H4, Canada
[36] Institució Catalana de Recerca i Estudis Avançats, Passeig de Lluís Companys, 23, 08010 Barcelona, Spain
[37] Institut de Física d'Altes Energies (IFAE), The Barcelona Institute of Science and Technology, Edifici Cn, Campus UAB, 08193, Bellaterra (Barcelona), Spain
[38] IRFU, CEA, Université Paris-Saclay, F-91191 Gif-sur-Yvette, France
[39] Instituto de Astrofísica de Andalucía (CSIC), Glorieta de la Astronomía, s/n, E-18008 Granada, Spain
[40] Departament de Física, EEBE, Universitat Politècnica de Catalunya, c/Eduard Maristany 10, 08930 Barcelona, Spain
[41] Department of Physics and Astronomy, Sejong University, 209 Neungdong-ro, Gwangjin-gu, Seoul 05006, Republic of Korea
[42] CIEMAT, Avenida Complutense 40, E-28040 Madrid, Spain
[43] Department of Physics, University of Michigan, 450 Church Street, Ann Arbor, MI 48109, USA
[44] National Astronomical Observatories, Chinese Academy of Sciences, A20 Datun Road, Chaoyang District, Beijing, 100101, P. R. China

Submitted to ApJ

ABSTRACT

The Milky Way Survey of the Dark Energy Spectroscopic Instrument (DESI) has so far observed three classical dwarf spheroidal galaxies (dSphs): Draco, Sextans and Ursa Minor. Based on the observed line-of-sight velocities and metallicities of their member stars, we apply the axisymmetric Jeans Anisotropic Multi-Gaussian Expansion modeling (JAM) approach to recover their inner dark matter distributions. In particular, both the traditional single-population Jeans model and the multiple population chemodynamical model are adopted. With the chemodynamical model, we divide member stars of each dSph into metal-rich and metal-poor populations. The metal-rich populations are more centrally concentrated and dynamically colder, featuring lower velocity dispersion profiles than the metal-poor populations. We find a diversity of the inner density slopes γ of dark matter halos, with the best constraints by single-population or chemodynamical models consistent with each other. The inner density slopes are $0.71^{+0.34}_{-0.35}$, $0.26^{+0.22}_{-0.12}$ and $0.33^{+0.20}_{-0.16}$ for Draco, Sextans and Ursa Minor, respectively. We also present the measured astrophysical J and D factors of the three dSphs. Our results indicate that the study of the dark matter content of dSphs through stellar kinematics is still subject to uncertainties behind both the methodology and the observed data, through comparisons with previous measurements and data sets.

1. INTRODUCTION

The standard Λ cold dark matter (ΛCDM) cosmological model has successfully predicted the distribution of large-scale structures in our Universe (e.g. Yang et al. 2004; Cole et al. 2005; Eisenstein et al. 2005; Henriques et al. 2012; Dawson et al. 2013; Han et al. 2015; Wang et al. 2016; Springel et al. 2018; DESI Collaboration et al. 2024a). On small scales and within dark matter halos, there have been discrepancies between predictions of the standard cosmological model and observations (see Bullock & Boylan-Kolchin 2017, for a review). One of the most hotly debated issues is the core-cusp problem (e.g. Flores & Primack 1994; Moore 1994; Burkert 1995; de Blok et al. 2001; Gentile et al. 2004; Gilmore et al. 2007; de Blok 2010; Oh et al. 2011). Cold dark matter simulations predict a universal density profile for dark matter halos with inner slopes close to 1 (cusp). By contrast, observations of low surface brightness galaxies, gas-rich dwarfs and dwarf spheroidal galaxies (dSphs) sometimes indicate inner density slopes close to 0 (core).

To understand the core-cusp problem, different scenarios have been proposed. Explanations beyond the ΛCDM theory turn to alternative dark matter models, such as self-interacting dark matter (e.g. Spergel & Steinhardt 2000; Rocha et al. 2013; Oman et al. 2015; Foot & Vagnozzi 2015; Kaplinghat et al. 2016; Jiang et al. 2023) and fuzzy dark matter (e.g. Hu et al. 2000; Hui et al. 2017). Within the CDM framework, stellar feedback is believed to be the most promising explanation, that repeated supernovae explosions move dark matter to more extended orbits and lower their densities in central regions (e.g. Navarro et al. 1996a; Read & Gilmore 2005; Read et al. 2019; Freundlich et al. 2020a; Li et al. 2023; Boldrini 2021). Numerical simulations have shown supporting evidences for this explanation (e.g. Mashchenko et al. 2008; Pontzen & Governato 2012, 2014). Observationally, Read et al. (2019) reported an anti-correlation between the inner dark matter densities of dwarf galaxies and their stellar-to-halo mass ratios, which supports the stellar feedback scenario from observations (Di Cintio et al. 2014). Hayashi et al. (2020) summarized that the relation between the inner dark matter density slopes of classical dwarf galaxies and their stellar-to-halo mass ratios generally agrees with re-

cent hydrodynamical simulations (e.g. Tollet et al. 2016; Freundlich et al. 2020b; Lazar et al. 2020).

However, the constraints on the inner dark matter densities for dSphs are still limited by statistical errors (Zhu et al. 2016a) and systematic uncertainties behind dynamical modeling (Genina et al. 2018; Wang et al. 2022, 2023). For example, Read et al. (2019) and Hayashi et al. (2020) both measured the inner dark matter densities for eight classical dSphs, utilizing spherical and axisymmetric Jeans analysis respectively, but their measurements are not fully consistent with each other. In fact, cuspy dSphs can be biased to be cored due to violations of steady-state and/or spherical assumptions (Genina et al. 2018; Wang et al. 2022). Besides, binary orbital motions can inflate the overall velocity dispersion, whereas deflate the very central densities of dSphs in dynamical modeling (Wang et al. 2023), though the change is not significant for classical dSphs.

The Milky Way dSphs are close enough to collect kinematical data of individual member stars for dynamical modeling. Recent observations have revealed the coexistence of multiple stellar populations in these systems (e.g. Tolstoy et al. 2004; Battaglia et al. 2008; Amorisco & Evans 2012a; Pace et al. 2020; Arroyo-Polonio et al. 2024). Many studies model the stellar kinematics of different populations simultaneously to constrain the inner dark matter distributions in several dSphs (Battaglia et al. 2008; Walker & Peñarrubia 2011; Amorisco & Evans 2012b; Agnello & Evans 2012; Amorisco et al. 2013; Zhu et al. 2016a; Strigari et al. 2017; Hayashi et al. 2018; Pace et al. 2020). For example, Walker & Peñarrubia (2011) estimate the slopes of mass profiles for Fornax and Sculptor defined by masses enclosed within half-number radii of two stellar populations, and found that their results are consistent with cored dark matter halos. In this study, we use the chemodynamical model developed in Zhu et al. (2016a) and Zhu et al. (2016b), which extends the discrete axisymmetric Jeans Anisotropic Multi-Gaussian Expansion (JAM) model (Watkins et al. 2013). Specifically, we will adopt both the single-population JAM model and a chemodynamical model in our analysis.

We mainly use spectroscopic data for member stars in dSphs from the Milky Way Survey (MWS) of the Dark Energy Spectroscopic Instrument (DESI). DESI is currently one of the leading multi-object spectrographs for wide-field surveys (Levi et al. 2013; DESI Collaboration et al. 2016a,b, 2022; Silber et al. 2023; Schlafly et al. 2023; DESI Collaboration et al. 2024b). The Early Data Release (EDR; DESI Collaboration et al. 2024c) and Data Release 1 (DR1) of the first year observation (DESI Collaboration et al. 2025a) have already been publically available. DESI primarily focuses on observations of distant galaxies for extra-galactic science, such as exploring the nature of dark energy and mapping the large-scale structure of our Universe (DESI Collaboration et al. 2024a; Adame et al. 2025a; DESI Collaboration et al. 2024d,e; Adame et al. 2025b; DESI Collaboration et al. 2024f, 2025b). DESI MWS also observes millions of stars within the Milky Way to better understand our Galaxy (Cooper et al. 2023). The Year-3 data of DESI MWS includes member stars in Draco, Sextans and Ursa Minor.

The paper is organized as follows. We first introduce spectroscopic data from DESI MWS for three dSphs and member star selection in Section 2. The single-population and chemodynamical model are described in Section 3. We present our results in Section 4, including measurements of the Astrophysical factors for dark matter detections. We compare with previous measurements in Section 5, including discussions on the core-cusp problem and selection effects. We draw conclusions in the end (Section 6).

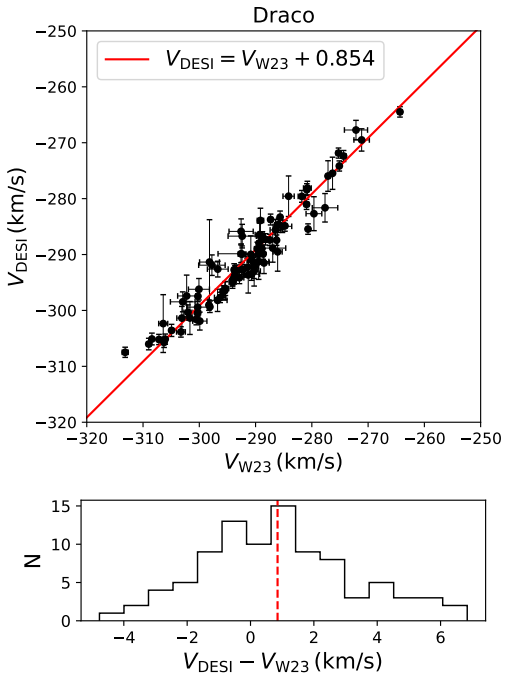

Figure 1. Top: A comparison between the Draco member star LOSV measurements by DESI MWS (y-axis) and in Walker et al. (2023) (x-axis). The red line is the best fit with slope of 1, and its y-intercept is the offset between two observations (see the legend). **Bottom:** The histogram of the differences between the LOSV measurements by DESI MWS and Walker et al. (2023). The red dashed vertical line represents the offset between two observations.

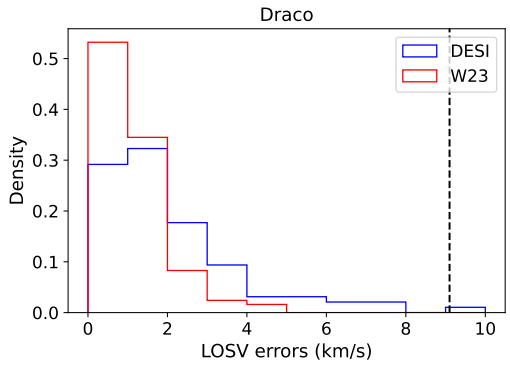

Figure 2. Distributions of LOSV errors for Draco member stars, observed by DESI MWS (blue) or by Walker et al. (2023) (red). The black vertical dashed line is the intrinsic LOSV dispersion of Draco (see Table 1).

2. DATA

2.1. *The DESI Milky Way Survey*

The Dark Energy Spectroscopic Instrument (DESI) is currently one of the leading multi-object spectrographs for wide-field surveys (DESI Collaboration et al. 2016a,b, 2022, 2024c). The survey is carried on the Mayall 4 meter telescope at the Kitt Peak National Observatory (Miller et al. 2024; Poppett et al. 2024), with 5,000 fibers allocated over a 3.2° diameter field of view at the prime focus. Although primarily focusing on observations of distant galaxies, DESI also collects spectroscopic data for stars within our Milky Way. The DESI Milky Way Survey (MWS) mainly operates during bright time, which refers to nights with more significant moon light contamination (Cooper et al. 2023; Koposov et al. 2024). The main survey of MWS will observe approximately seven million stars. DESI MWS also has extra secondary targets, such as faint blue horizontal branch stars (BHBs) in addition to those observed in the main survey. Beyond main survey and secondary targets, DESI MWS has tertiary programs, with dedicated fibers to observe special targets such as individual dSphs and stellar streams. In this work, we utilize the internal Year-3 data of DESI MWS, which covers data from the first three-year of observations. Note the DESI Year-1 data, commissioning and Science Validation (SV) data (DESI Collaboration et al. 2024b), which are already published in DESI DR1 (Koposov et al. 2025) and EDR (DESI Collaboration et al. 2024c; Koposov et al. 2024), are included in the latest internal version of Year-3 data.

2.2. *DESI observations of Draco, Sextans and Ursa Minor*

So far, DESI MWS has observed stars in footprints of three dSphs: Draco, Sextans and Ursa Minor (UMi). The properties of the three dSphs are summarized in Table 1. Nearly 85% and 30% of the data for Draco and Sextans are taken from the SV, with the remaining from the main survey after SV. The data for UMi are from the tertiary program, instead of from the main survey. We use the line-of-sight velocity (LOSV) and metallicity measurements of observed stars output by the DESI MWS `RVS` pipeline. The readers can find more details about the pipeline in Cooper et al. (2023) and Koposov et al. (2024). We select stars with `RVS_WARN` = 0 to ensure the robustness of the stellar model fit by the pipeline[1]. For stars with repeated observations in different programs, we use the observation with the smallest error of the LOSV measurement. Note for the LOSV errors reported by `RVS`, there is an additional systematic component or error floor of 0.9 km/s, as mentioned in Cooper et al. (2023). We add this systematic error in quadrature to the LOSV errors in our analysis.

2.3. *Observations from Walker et al. (2023)*

We combine the DESI MWS data for three dSphs with the spectroscopic data from Walker et al. (2023), which are based on Magellan/M2FS and MMT/Hectochelle observations. Since some stars have multi-epoch observations in this data set by Walker et al. (2023), for each star we adopt the mean value of the LOSV (vlos_mean) and metallicity (feh_mean) measurements. The LOSV measurements by DESI and by Walker et al. (2023), however, may subject to different zero points, and we use stars observed by both DESI and Walker et al. (2023) to correct for this systematic offset. We show the LOSVs of stars observed by both DESI and Walker et al. (2023) and in the footprint of Draco as an example in Figure 1. There is an overall good agreement between the LOSV measurements by DESI and by Walker et al. (2023), with the data points in the top panel go well through the red diagonal line, but the LOSV measured by Walker et al. (2023) of Draco is on average lower than that of DESI by about 1 km/s , which is also obvious in the histogram of the differences in the bottom panel. This offset is added to the measurements of Walker et al. (2023).

For these stars that exist in both DESI and Walker et al. (2023), we use the LOSV measured with the

[1] `RVS_WARN` is a bitmask flag output by the `RVS` pipeline, which indicates potential issues or warnings in the LOSV measurements and stellar parameter determinations. The first bit of `RVS_WARN` is set to 1 if the difference in the χ^2 values between the best-fit stellar model and the continuum model is small. The second bit is set to 1 if the LOSV is within 5 km/s of the predefined velocity boundary (−1500 to 1500 km/s). The third bit is set to 1, if the LOSV uncertainty exceeds 100 km/s. A spectrum without any of these concerns is indicated by `RVS_WARN` = 0

smaller error. In Figure 2, we show the LOSV error distributions of stars in Draco, observed by DESI or in Walker et al. (2023). In general, LOSV measurements from DESI have larger errors than those from Walker et al. (2023), but both of them are smaller than the intrinsic LOSV dispersion of Draco (black dashed vertical line, from Pace et al. (2022)), indicating that they can be used for proper dynamical modeling. For metallicity measurements, we also adopt the one with the smaller measurement error for stars existing in both DESI and Walker et al. (2023), and we have corrected the mean offset of metallicity measurements by Walker et al. (2023) from those of DESI.

2.4. *Member star selection*

To select actual member stars for the three dSphs, we utilize the membership catalog for dwarf galaxies by Pace et al. (2022). The membership probabilities for stars associated to known MW dwarf galaxies are calculated by Pace et al. (2022) according to their *Gaia* parallaxes and spatial distributions, with a projected Plummer model adopted as the prior for the spatial distribution. Specifically, we first select stars with the probability `mem_fixed` or `mem_fixed_complete` greater than 0.9 from the membership catalog of Pace et al. (2022). We cross match the sample of stars observed by DESI in the footprints of the three dSphs or in Walker et al. (2023) to these high probability member stars, to obtain our sample of spectroscopically observed member stars. The matching is based on a searching radius of 0.3 arcsec. In the end, we further include 3σ clippings to the LOSVs and metallicities to further discard stars that are at the tail of the LOSV and metallicity distributions, which are possible contaminations. For LOSV, we use the systemic LOSV and its dispersion in Table 1 to set the 3σ boundaries for each dSphs. For metallicity we use the mean and standard deviation of our samples to set the 3σ boundaries. We also discard stars beyond 2.5 half-light radius from the center of each dSphs to further exclude possible contaminations and dwarf halo stars (e.g. Deason et al. 2022).

In our analysis, the central coordinates and systemic velocities of each dwarf galaxy have been subtracted from the observed coordinates and velocities for each member star in Cartesian coordinates, to correct the perspective rotation (Feast et al. 1961). The central coordinates and systemic proper motions for three dSphs are provided in Table 1. The systemic LOSV of each dSph is the mean LOSV of its member stars selected above.

For each individual member star, not only their LOSVs are used for dynamical model, but also their *Gaia* proper motions are used. However, at the distances of the three dSphs used in our analysis, the uncertainties in *Gaia* proper motion measurements are quite large. Nevertheless, we still incorporated proper motions in our dynamical modeling, with the observational uncertainties for both LOSV and proper motions properly incorporated in the likelihood function (see Section 3.1 below), which will be taken into account by the model. Notably, we report the total velocity dispersion when comparing the actual and model predicted velocity dispersions instead of the intrinsic velocity dispersions deconvolved from observational errors.

Though the pulsating velocities of DESI RR Lyraes have been corrected (Medina et al. 2025a,b)[2], we want to eliminate the possibility that some faint RR Lyraes may still remain unidentified to inflate the velocity dispersions of our dSphs. For safety, we exclude all member stars along the horizontal branch from our sample to remove potential faint RR Lyraes. We do not exclude possible binary stars since the effect of binary stars to inflate the velocity dispersion of classical dSph is very minor (e.g. Hargreaves et al. 1996; Minor et al. 2010; Spencer et al. 2017; Wang et al. 2023). We provide in Table 2 the final number of member stars in the three dSphs after our selections above, with the number of stars observed by DESI or in Walker et al. (2023) provided as well.

3. METHOD

We introduce both single-population and two-population chemodynamical models in this section.

3.1. *Single-population model*

Our single-population model is the axisymmetric Jeans Anisotropic Multi-Gaussian Expansion (JAM) modeling method (Cappellari 2008; Watkins et al. 2013). JAM is an open source code[3], and in this study we use a slightly different version by Zhu et al. (2016a) and Zhu et al. (2016b), with improved python interfaces and plotting tools.

Under the axisymmetric and steady-state assumptions, the Jeans equations in cylindrical coordinates are

$$\frac{\nu\left(\overline{v_R^2}-\overline{v_\phi^2}\right)}{R}+\frac{\partial\left(\nu\overline{v_R^2}\right)}{\partial R}+\frac{\partial\left(\nu\overline{v_R v_z}\right)}{\partial z}=-\nu\frac{\partial\Phi}{\partial R}, \quad (1)$$

$$\frac{\nu\overline{v_R v_z}}{R}+\frac{\partial\left(\nu\overline{v_R v_z}\right)}{\partial R}+\frac{\partial\left(\nu\overline{v_z^2}\right)}{\partial z}=-\nu\frac{\partial\Phi}{\partial z}, \quad (2)$$

[2] The DESI MWS RRL targets are based on the *Gaia* Data Release 2 (DR2; Clementini et al. 2019) and the Pan-STARRS1 (PS-1; Sesar et al. 2017) catalogs.

[3] https://github.com/lauralwatkins/cjam

dSph	α_0 [deg]	δ_0 [deg]	$r_{\rm h}$ [arcmin]	$\mu_{\alpha\star}$ [mas yr^{-1}]	μ_δ [mas yr^{-1}]	d [kpc]	$v_{\rm los}$ [km s^{-1}]	$\sigma_{\rm los}$ [km s^{-1}]
Draco	260.0684	57.9185	9.67 ± 0.09	0.044	-0.188	76	-290.7	9.1 ± 1.2
Sextans	153.2628	-1.6133	16.50 ± 0.10	-0.409	0.037	86	224.3	7.9 ± 1.3
UMi	227.242	67.2221	18.30 ± 0.11	-0.120	0.071	76	-247.0	8.6 ± 0.3

Table 1. A summary of the central sky coordinates in Equatorial coordinates (α_0 and δ_0), half-light radii (r_h), systemic proper motions ($\mu_\alpha*$ and μ_δ), distances (d), systemic LOSVs ($v_{\rm los}$), and intrinsic LOSV dispersions ($\sigma_{\rm los}$) for the three dSphs (Draco, Sextans and UMi) used in the analysis of this paper. All of the information are taken from Pace et al. (2022), except for the distances, which are taken from Muñoz et al. (2018).

Object	$N_{\rm tot}$	$N_{\rm DESI}$	$N_{\rm W23}$
Draco	407	96	374
Sextans	440	240	368
UMi	1046	1003	416

Table 2. Numbers of member stars in the three dSphs used in our analysis. $N_{\rm tot}$ is the total number of member stars after selections in Section 2.4. $N_{\rm DESI}$ and $N_{\rm W23}$ are the numbers of member stars which are observed by DESI and from Walker et al. (2023), respectively. There are overlaps between the observed stars by DESI and in Walker et al. (2023), and for those stars existing in both data set, we use the LOSV and metallicity measurements with smaller errors (see Section 2.3).

where ν represents the tracer number density distribution and Φ represents the total gravitational potential.

To obtain unique solutions to the Jeans equations, we further assume that the velocity ellipsoid is aligned with the cylindrical coordinates, so the cross-term can be neglected, i.e., $\overline{v_R v_z} = 0$. Besides, the velocity anisotropy, defined as $\beta_z = 1 - \overline{v_z^2}/\overline{v_R^2}$, is assumed to be constant. Moreover, to calculate the first velocity moments, a rotation parameter κ is defined as $\overline{v_\phi} = \kappa|\overline{v_\phi^2} - \overline{v_R^2}|^{1/2}$, which we also assume to be constant. Note our κ follows the modified definition of Zhu et al. (2016a).

The gravitational potential (Φ) in Equation 1 and 2 is contributed by both luminous and dark matter. For dark matter, we adopt the generalized NFW (Navarro et al. 1995, 1996b, 1997) (gNFW) model profile

$$\rho(r) = \frac{\rho_s}{(r/r_s)^\gamma (1 + r/r_s)^{(\alpha-\gamma)}}, \tag{3}$$

where ρ_s is the scale density, r_s is the scale radius, γ and α are inner and outer density slopes, respectively. In our analysis we consider spherical dark matter halos. Moreover, because the number of member stars in outskirts is much less, our constraints on the outer density slope, α, are very weak, and thus we fix α to 4 throughout the paper. We choose 4 instead of 3 because the outskirts of dSphs have undergone tidal effects so their profiles become steeper. However, we have verified that our constraints on the inner density profiles are not sensitive to the chosen value of the outer slope, and the constraints on the inner density profiles do not change as well if we make α a free parameter (also see Wang et al. 2022).

For the luminous matter, i.e., member stars, the gravitational potential is obtained by deprojecting the density map based on the inclination angle. The density map is estimated by multiplying the observed surface brightness map by the stellar mass-to-light ratio (M_*/L_*). Here M_*/L_* is determined from the closest matched PARSEC isochrone (Bressan et al. 2012)[4]. To obtain the surface brightness map, we create a projected image for each dSph using membership catalogs constructed in Section 2.4, with each member star weighted by its luminosity. To account for faint stars with magnitudes below the *Gaia* flux limit, we scale the surface brightness map up to bring the integrated luminosity equal to the total luminosity of each dSph from Muñoz et al. (2018).

In addition to the dark and luminous potential, there is the tracer surface number density term (ν) in Equations 1 and 2. In principle, ν can be deprojected from the surface number density maps of member stars with spectroscopic observations, which are used as tracers. Note, however, for each dSph only a subset of stars in the full membership catalog constructed in Section 2.4 have spectroscopic observations due to fiber collisions. Especially in central regions of dSphs, where the surface number density of stars is very high, the completeness fraction of spectroscopically observed stars versus targets is much lower (e.g. Ding, et al., submitted). Thus instead of using the surface number density maps of spectroscopically observed member stars, ν is deprojected from the surface number density maps of all target stars in the full membership catalog in Section 2.4. We do not include any scaling on the amplitude of ν, as it cancels out on both sides of the Jeans Equations.

We show the surface number density profiles of all target member stars (black squares) and spectroscopically

[4] http://stev.oapd.inaf.it/cmd

observed member stars (black triangles) in concentric elliptical radial bins in Figure 3. For each dSph in the upper panels, the projected axis ratio q' is obtained from the surface number density map and remains the same for different elliptical bins. The dashed curves in the upper panels are the Multi-Gaussian Expansions to these profiles, which will be introduced later. In the bottom panels, the completeness fractions for the spectroscopically observed member stars with respect to the targets in each dSphs are also shown. It can be seen that the completeness fractions are lower in the denser central regions due to unassigned fibers. Here the completeness fractions for Draco are different from those in Ding, et al., submitted, since we combine DESI MWS data with those from Walker et al. (2023) and remove stars on the horizontal branch.

Although the spatial distributions of spectroscopically observed member stars and the full member star sample differ, we assume they do not differ in the velocity moment profiles, so the dynamical modeling outcome is not affected due to the incompleteness in fiber assignments. Equivalently, we are assuming that the spectroscopically observed member stars at different projected radii to the dSph center are a random subset in velocity space of the full sample. This is a reasonable assumption if the fiber assignment does not depend on any velocity information. However, as we have seen in Figure 3, the tiling and fiber completeness fraction differ in the central regions and the outskirts. In addition, metal-rich stars have more concentrated radial distributions to the dSph center, and the kinematics of metal-rich and metal-poor stars can differ. The fiber assignments may depend on member star kinematics. Unfortunately, if such a selection bias exists, it is hard to incorporate corrections, because we do not have LOSV measurements for the full target sample. We choose to adopt the assumption for the main results of our current paper, with detailed discussions provided in Section 5 to discuss such selection effects.

In order to have quick analytical solutions to the Jeans equations, the Multi-Gaussian Expansion (MGE) approach is applied to decompose the surface number density maps of tracers, the surface density maps of luminous matter, and the gravitational potential of the dark matter profile into different Gaussian components. Each Gaussian component can be easily deprojected to get the corresponding analytical form in 3-dimensions. For example, the surface number density map of tracers $\Sigma(x', y')$ can be decomposed as

$$\Sigma(x', y') = \sum_j \frac{L_j}{2\pi\sigma_j^2 q'_j} \exp\left[-\frac{1}{2\sigma_j^2}\left(x'^2 + \frac{y'^2}{q'^2_j}\right)\right], \quad (4)$$

where L_j, σ_j and q'_j are the total number density, dispersion and projected axis ratio of each Gaussian component j. The corresponding 3-dimensional tracer number density distribution $\nu(R, z)$ (in cylindrical coordinates) can be simply deprojected as

$$\nu(R, z) = \sum_j \frac{L_j}{(2\pi\sigma_j^2)^{3/2} q_j} \exp\left[-\frac{1}{2\sigma_j^2}\left(R^2 + \frac{z^2}{q_j^2}\right)\right] \quad (5)$$

for each Gaussian component. Here q_j is the intrinsic axis ratio and can be linked to the projected axis ratio q'_j through the inclination angle i of the dSph

$$q_j = \frac{\sqrt{q'^2_j - \cos^2 i}}{\sin i}. \quad (6)$$

Note that the inclination angle i is defined as the angle between the normal vector of the dSph and the line of sight, where $i = 0$ corresponds to a face-on orientation.

Since the surface number density map is noisy, in practice we fit 1-dimensional MGE to surface number density profiles in Figure 3 to obtain L_j and σ_j for each Gaussian component j in Equation 4. This is done in bins of concentric elliptical isophotes with the same axis ratio and orientation. Then these 1-dimensional MGE can be extended to 2-dimensional MGE by adding the projected axis ratio q'_j to each Gaussian component. q'_j is the axis ratio of the entire dwarf galaxies. Here we are assuming that different Gaussian components have the same axis ratio, which is a reasonable assumption based on the projected map of the three dSphs. We show the 1-dimensional MGE components for three dSphs in Figure 3 as colored dashed curves, and the black solid curve denotes the summation of these MGE components. The parameters of each MGE component and for the three dSphs are shown in Table 3. In all three dSphs, black solid curves provide good matches to black squares, which are surface number density profiles of all targeted member stars.

In the end, the final solution of the velocity moments is the summation of the analytical solution of each MGE component. In principle, the velocity anisotropy, β_z, and the rotation parameter, κ, can vary with different MGE components, but in this paper we assume that they are the same for all MGE components.

The above analytical solutions are first obtained in the intrinsic coordinates of the dSph, and then transformed to the observed frame to be compared with observational data. The coordinate system in the observed frame (x', y', z') is a left-handed system. The x'-axis lies along the projected major axis of the observed image of the galaxy, which is required by the MGE approach, and

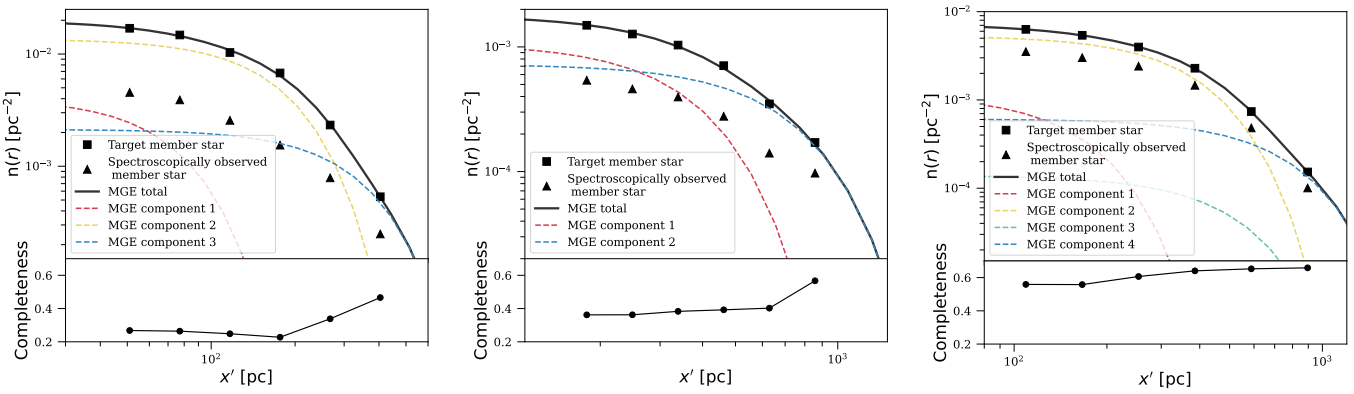

(a) Draco (b) Sextans (c) UMi

Figure 3. Top panel: Surface number density profiles of targets and spectroscopically observed member stars along the major axis, x', for each dSph. The black squares and triangles are mean surface number densities in elliptical isophotal radial bins of targets and spectroscopically observed member stars. The colored dashed curves represent different MGE components, and the black solid curves are the summations of these MGE components, which match well the black squares. **Bottom panel:** The completeness fraction of spectroscopically observed member stars versus targets, as a function of the projected distance along the major axis. The left, middle and right panels are for Draco, Sextans and UMi, respectively.

Object	j	L_j [10^{-4}pc^{-2}]	σ_j [pc]	q'_j
Draco	1	40.27	50.99	0.65
	2	136.26	122.48	0.65
	3	21.27	233.47	0.65
Sextans	1	10.65	253.38	0.70
	2	7.26	494.93	0.70
UMi	1	11.45	109.15	0.49
	2	53.41	256.90	0.49
	3	1.40	345.72	0.49
	4	6.08	517.06	0.49

Table 3. Parameters of MGE for surface number density profiles of three dSphs. For each Gaussian component j, L_j is the total number density, σ_j is the dispersion along the major axis, and q'_j is the projected axis ratio.

the y'-axis lies along the projected minor axis. The z'-axis is aligned with the line-of-sight direction, pointing away from us. On the other hand, the coordinate system in the intrinsic frame (x, y, z) is a right-handed system. The x-axis coincides with the x'-axis of the coordinates in the observed frame, and two coordinate systems are linked via

$$\begin{pmatrix} x' \\ y' \\ z' \end{pmatrix} = \begin{pmatrix} 1 & 0 & 0 \\ 0 & -\cos i & \sin i \\ 0 & \sin i & \cos i \end{pmatrix} \begin{pmatrix} x \\ y \\ z \end{pmatrix}, \tag{7}$$

where i is the inclination angle of the galaxy.

We use a maximum-likelihood analysis to find the model that best describes our discrete data set. For a star located at $\boldsymbol{x}'_i = (x'_i, y'_i)$ on the plane of the sky, it has the velocity vector $\boldsymbol{v}_i = (v_{x',i},\, v_{y',i},\, v_{z',i})$ and the error matrix

$$\boldsymbol{S}_i = \begin{pmatrix} \sigma^2_{v_{x'},i} & 0 & 0 \\ 0 & \sigma^2_{v_{y'},i} & 0 \\ 0 & 0 & \sigma^2_{v_{z'},i} \end{pmatrix}, \tag{8}$$

where $\sigma_{v_{x'},i}$, $\sigma_{v_{y'},i}$ and $\sigma_{v_{z'},i}$ are observational errors of velocity components $v_{x',i}$, $v_{y',i}$ and $v_{z',i}$, respectively. Here the observational errors of $v_{x',i}$ and $v_{y',i}$ are obtained from their *Gaia* proper motion uncertainties. At the distances of the three classical dSphs, the proper motion uncertainties are very large, so the major constraints are contributed by the LOSVs. We have checked that including or not including *Gaia* proper motions for dSph member stars lead to almost the same results. Based on a set of parameters Θ, the model predicts a mean velocity vector $\boldsymbol{\mu}_i = (\overline{u_{x',i}},\, \overline{u_{y',i}},\, \overline{u_{z',i}})$ with a covariance matrix

$$\boldsymbol{C}_i = \begin{pmatrix} \overline{u^2_{x'}} - \overline{u_{x'}}^2 & \overline{u^2_{x'y'}} - \overline{u_{x'}u_{y'}} & \overline{u^2_{x'z'}} - \overline{u_{x'}u_{z'}} \\ \overline{u^2_{x'y'}} - \overline{u_{x'}u_{y'}} & \overline{u^2_{y'}} - \overline{u_{y'}}^2 & \overline{u^2_{y'z'}} - \overline{u_{y'}u_{z'}} \\ \overline{u^2_{x'z'}} - \overline{u_{x'}u_{z'}} & \overline{u^2_{y'z'}} - \overline{u_{y'}u_{z'}} & \overline{u^2_{z'}} - \overline{u_{z'}}^2 \end{pmatrix} \tag{9}$$

at the projected position of this star. By assuming that the velocity distribution predicted by the model is a trivariate Gaussian with the mean velocity $\boldsymbol{\mu}_i$ and the covariance $\boldsymbol{C}_i$, the likelihood for each star can be expressed as

$$\begin{aligned} L_i &= p\left(\boldsymbol{v}_i \mid \boldsymbol{x'}_i, \boldsymbol{S}_i, \boldsymbol{\mu}_i, \boldsymbol{C}_i\right) \\ &= \frac{\exp\left[-\frac{1}{2}\left(\boldsymbol{v}_i - \boldsymbol{\mu}_i\right)^{\mathrm{T}}\left(\boldsymbol{C}_i + \boldsymbol{S}_i\right)^{-1}\left(\boldsymbol{v}_i - \boldsymbol{\mu}_i\right)\right]}{\sqrt{(2\pi)^3 \left|\left(\boldsymbol{C}_i + \boldsymbol{S}_i\right)\right|}}. \end{aligned} \tag{10}$$

Then the total likelihood, defined as the product of likelihoods for all N stars, is

$$L = \prod_{i=1}^{N} L_i \ . \tag{11}$$

There are six free parameters in our single-population model, and their priors are:

1. Scale density of the dark matter halo, ρ_s: uniform distribution over $-15 \leq \log_{10}[\rho_s/(\mathrm{M}_\odot\,\mathrm{pc}^{-3})] \leq 15$;
2. Scale radius of the dark matter halo, r_s: uniform distribution over $0.1 \leq r_s/(\mathrm{kpc}) \leq 10$;
3. Inner density slope of the dark matter halo, γ: uniform distribution over $0.1 \leq \gamma \leq 4$;
4. Inclination angle of the galaxy, i: uniform distribution over $\cos^{-1}(q') < i/\mathrm{deg} \leq 90$;
5. Velocity anisotropy, β_z: uniform distribution over $-\infty < -\ln(1-\beta_z) < +\infty$;
6. Rotation parameter, κ: uniform distribution over $-\infty < \kappa < +\infty$.

In particular, to improve the efficiency of exploring the parameter space for ρ_s and r_s, we fit redefined parameters $d_1 = \log_{10}\rho_s^2 r_s^3$ and $d_2 = \log_{10}\rho_s$ instead. In addition, the velocity anisotropy β_z is symmetrically transformed as $\lambda = -\ln(1-\beta_z)$.

3.2. *Chemodynamical model*

For our chemodynamical model, we follow the approach in Zhu et al. (2016a,b). In general, for systems with k different stellar populations, each population features distinct spatial, chemical and dynamical properties, but all trace the same gravitational potential. Specifically, here we consider $k = 2$ stellar populations, composed of a metal-poor population and a metal-rich population. We consider chemical, spatial and dynamical probabilities for each star.

3.2.1. *Spatial probability*

For the star i observed at (x_i', y_i'), the conditional probability of it belonging to population k is defined as

$$P_{\mathrm{spa},i}(k|x_i', y_i') = \frac{\Sigma^k(x_i', y_i')}{\Sigma_{\mathrm{tot}}(x_i', y_i')}, \tag{12}$$

where the total surface number density $\Sigma_{\mathrm{tot}}(x', y')$ is the superposition of the surface number densities of two populations: $\Sigma_{\mathrm{tot}} = \Sigma^{\mathrm{metal-poor}} + \Sigma^{\mathrm{metal-rich}}$.

To calculate the spatial probability, we need to construct the surface number density map for each population. If the maps of two populations are left completely free, there may be too many parameters which are difficult for our model to constrain. To reduce the number of free parameters, we first construct two template maps, and the surface number density maps of two populations are assumed to be linear combinations of these two template maps.

To construct the template maps, we first apply a simple hard cut in metallicity to divide spectroscopically observed member stars into two template populations. This hard cut is chosen to maximize[5] the half-number radii[6] difference between the two template populations after the division. Next we compute the surface number density maps of the two template populations defined by this hard cut, with the maps fixed as template maps. We call the two templates as red and blue. Note, however, the template maps created in this way are subject to incompleteness due to fiber collisions, and the completeness fraction is lower in more central regions where the surface number density of target member stars is higher. To correct for the incompleteness, we first calculate the completeness fraction map according to the ratios of the surface number density maps between spectroscopically observed member stars and the full sample of target stars in the membership catalog (see Section 2.4). We multiply the red and blue template maps by the inverse of the completeness fraction map to correct for the incompleteness. The completeness fraction map is the same for both templates, as without spectroscopic metallicity measurements for target stars without fiber assignments, it is impossible for us to divide them into two populations.

After constructing the template maps, the surface number density map of each population in the chemodynamical model is the linear combination of these two template maps. For example, the surface number density map of the metal-poor population $\Sigma^{\mathrm{metal-poor}}$ can be written as

$$\Sigma^{\mathrm{metal-poor}}(x', y') = h_1 \Sigma^{\mathrm{red}}_{\mathrm{template}}(x', y') + h_2 \Sigma^{\mathrm{blue}}_{\mathrm{template}}(x', y')\,, \tag{13}$$

where $\Sigma^{\mathrm{red}}_{\mathrm{template}}$ and $\Sigma^{\mathrm{blue}}_{\mathrm{template}}$ denote two template maps, and the fractions h_1 and h_2 will be left as free parameters. Since any two populations are divided from the total sample, we have $\Sigma_{\mathrm{tot}} = \Sigma^{\mathrm{metal-poor}} + \Sigma^{\mathrm{metal-rich}} =$

[5] We have also tried different choices of hard cuts, such as the cuts that leave some gap in between the two populations, so that they are more separated. Our best constrained model profiles remain almost the same.

[6] The radius within which it includes half of the stars in the sample.

$\Sigma^{\rm blue}_{\rm template}+\Sigma^{\rm red}_{\rm template}$. Hence, the surface number density map of the metal-rich population in the chemodynamical model has the same form but with different fractions $1-h_1$ and $1-h_2$.

To create the red and blue template maps, a hard cut in metallicity is adopted above. In the end and with the best constrained chemodynamical model, we can calculate the probability for each star to be in the metal-rich or metal-poor populations, based on the joint posterior distribution combining spatial, kinematical and metallicity distributions (Equation 17 below). We call this a soft division. If the template maps are reasonable proxies for the maps of two populations, i.e., if the red/blue template is more metal-rich/metal-poor, the fractions are expected to be $h_1\sim 0$ and $h_2\sim 1$, and the hard and soft divisions would be close to each other.

We show the template maps for the three dSphs in Figure 4. The hard cuts in metallicity for the red and blue templates are -2.10, -1.87, -2.07 for Draco, Sextans and UMi, respectively. The red population has higher number densities in the inner region and lower densities in the outer region than the blue population. Thus, the hard cut in metallicity naturally leads to a more concentrated, metal-rich template population and a more extended, metal-poor template population in each dSph.

3.2.2. *Chemical probability*

We assume that the metallicity distribution of each population k follows a Gaussian distribution, characterized by the mean metallicity Z_0^k and the dispersion σ_Z^k. Thus, for the star i with the metallicity measurement $Z_i\pm\delta Z_i$, its chemical probability in the population k can be written as

$$P_{{\rm chm},i}(Z_i|k)=\frac{1}{\sqrt{2\pi[(\sigma_Z^k)^2+(\delta Z_i)^2]}}\exp\left[-\frac{1}{2}\frac{(Z_i-Z_0^k)^2}{[(\sigma_Z^k)^2+(\delta Z_i)^2]}\right]. \tag{14}$$

3.2.3. *Dynamical probability*

For each population, the dynamical probability follows that in the single-population model. Each population featuring distinct number density distribution ν_k satisfies the Jeans Equations for their own velocity moments, but both of them trace the same gravitational potential. The number density distribution of each population is deprojected from its surface number density map as mentioned in Section 3.2.1. For the star i with the velocity vector $\boldsymbol{v}_i=(v_{x',i},\,v_{y',i},\,v_{z',i})$ and the error matrix $\boldsymbol{S}_i$ (Equation 8 above), the dynamical probability of it being within the population k is

$$P_{{\rm dyn},i}(\boldsymbol{v}_i|k)=\frac{\exp\left[-\frac{1}{2}\left(\boldsymbol{v}_i-\boldsymbol{\mu}_i^k\right)^{\rm T}\left(\boldsymbol{C}_i^k+\boldsymbol{S}_i\right)^{-1}\left(\boldsymbol{v}_i-\boldsymbol{\mu}_i^k\right)\right]}{\sqrt{(2\pi)^3\left|\left(\boldsymbol{C}_i^k+\boldsymbol{S}_i\right)\right|}}, \tag{15}$$

where $\boldsymbol{\mu}_i^k$ and $\boldsymbol{C}_i^k$ (Equation 9 above) are the mean velocity and the covariance predicted at the position of the star by our model for each population, respectively. The velocity anisotropy β_z^k and the rotation parameter κ^k can vary between two populations, while they are still kept the same for all Gaussian components of each population.

3.2.4. *Joint probability*

For a star i at projected coordinate x' and y', its joint probability distribution of population type k, velocity $\boldsymbol{v}_i$ and metallicity Z_i is

$$P(k,\boldsymbol{v}_i,Z_i|x',y')=P_{{\rm dyn},i}(\boldsymbol{v}_i|k,x',y')P_{{\rm chm},i}(Z_i|k)P_{{\rm spa},i}(k|x',y')\,. \tag{16}$$

To separate stars into different populations in a given model, we use the relative value

$$P(k|\boldsymbol{v}_i,Z_i,x',y')=\frac{P(k,\boldsymbol{v}_i,Z_i|x',y')}{\sum_{k=1,2}P(k,\boldsymbol{v}_i,Z_i|x',y')}, \tag{17}$$

to represent the probability for the star i to be within the population k.

The likelihood of star i can be written as

$$L_i=\sum_{k=1,2}P_{{\rm dyn},i}(\boldsymbol{v}_i|k)P_{{\rm chm},i}(Z_i|k)P_{{\rm spa},i}(k|x',y'), \tag{18}$$

where $\sum_{k=1,2}P_{{\rm spa},i}(k|x',y')=1$ according to the definition of Equation 12 above.

Then the total likelihood for all N stars is

$$L=\prod_{i=1}^{N}L_i\,. \tag{19}$$

There are fourteen free parameters in our chemodynamical model, and their priors are:

1. Scale density of the dark matter halo, ρ_s: uniform distribution over $-15\le\log_{10}[\rho_s/({\rm M}_\odot\,{\rm pc}^{-3})]\le 15$;
2. Scale radius of the dark matter halo, r_s: uniform distribution over $0.1\le r_s/({\rm kpc})\le 10$;
3. Inner density slope of the dark matter halo, γ: uniform distribution over $0.1\le\gamma\le 4$;
4. Inclination angle of the galaxy, i: uniform distribution over $\cos^{-1}(q')<i/{\rm deg}\le 90$;

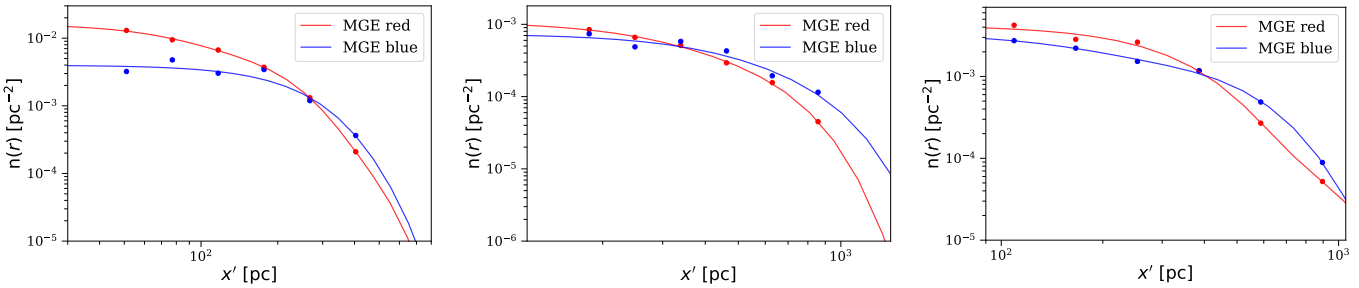

(a) Draco (b) Sextans (c) UMi

Figure 4. Surface number density profiles of two template maps along the major axis, x', for each dSph. The two template maps are obtained for the metal-rich (red) and metal-poor (blue) subpopulations after a hard cut in metallicity for the division, and the hard cut is chosen to maximize the difference in the half-number radii of the two populations. Red and blue dots are surface number densities directly calculated from corresponding template maps. Solid curves with the same colors as dots denote the reconstructed profiles from different MGEs. The left, middle and right panels are for Draco, Sextans and UMi, respectively.

5. Velocity anisotropies for the metal-rich population, $\beta_z^{\rm mr}$, and for the metal-poor population, $\beta_z^{\rm mp}$: uniform distribution over $-5 \leq -\ln(1-\beta_z^{\rm mr}) \leq +5$, $-5 \leq -\ln(1-\beta_z^{\rm mp}) \leq +5$;

6. Rotation parameters for the metal-rich population, $\kappa^{\rm mr}$, and for the metal-poor population, $\kappa^{\rm mp}$: uniform distribution over $-\infty < \kappa^{\rm mr} < +\infty$, $-\infty < \kappa^{\rm mp} < +\infty$;

7. Mean of metallicity distributions for the metal-rich population, $Z_0^{\rm mr}$, and for the metal-poor population, $Z_0^{\rm mp}$: uniform distribution over $-\infty < Z_0^{\rm mr} < +\infty$, $-\infty < Z_0^{\rm mp} < +\infty$;

8. Dispersion of metallicity distributions for the metal-rich population, $\sigma_Z^{\rm mr}$, and for the metal-poor population, $\sigma_Z^{\rm mp}$: uniform distribution over $0 \leq \sigma_Z^{\rm mr} < +\infty$, $0 \leq \sigma_Z^{\rm mp} < +\infty$;

9. Surface number density fractions for two template maps, h_1 and h_2: uniform distribution over $0 \leq h_1 \leq 1$, $0 \leq h_2 \leq 1$.

Similar to the single-population model, we fit $d_1 = \log_{10}\rho_s^2 r_s^3$ and $d_2 = \log_{10}\rho_s$ instead of ρ_s and r_s. Besides, velocity anisotropies $\beta_z^{\rm mr}$ and $\beta_z^{\rm mp}$ are transformed as $\lambda^{\rm mr} = -\ln(1-\beta_z^{\rm mr})$ and $\lambda^{\rm mp} = -\ln(1-\beta_z^{\rm mp})$ as well.

4. RESULTS

In this section, we present our results for both single-population and chemodynamical models. For each model, we show best-fit model parameters as well as best-fit velocity moments compared with the real observations. For the chemodynamical model, we also present the spatial, kinematical and metallicity distributions of the two populations separated by the best model. In the end, we calculate the astrophysical J and D factors for dark matter indirect detections.

4.1. *Best constraints and performance of the single-population model*

The best-fit parameters for the single-population model of the three dSphs are provided in Table 4. In Figure 5, we show these constraints for the single-population model by the magenta dots with errorbars. The green symbols denote those for the chemodynamical model, which will be discussed later in Section 4.2.

The likelihood contours for different parameters combinations in the single-population model are shown in Figure 6 for Draco only. The trends are similar for Sextans and UMi. Our model imposes weaker constraints on the inclination angle (i) compared to other parameters, which is indicated by its wide posterior distribution. The rotation parameter (κ) shows a weak correlation with the potential parameters (d_1, d_2 and γ), whereas there are strong degeneracies among the potential parameters themselves. The correlation between the velocity anisotropy (λ) and the other potential parameters is also present, which is the mass-anisotropy degeneracy.

The mass-anisotropy degeneracy can be weakened if we have precise proper motion measurements. However, at the distances of the three dSphs used in this paper, their *Gaia* proper motions used in our constraints are subject to very large errors, and as we have mentioned, including or not including *Gaia* proper motions in our analysis leads to very similar constraints. More precise proper motions can possibly be achieved by combining *Gaia* and previous observations by the Hubble Space Telescope (e.g. del Pino et al. 2022), but this is only available for a small number of stars in more central regions, and thus in this study we focus on using only *Gaia* proper motions.

The best recovered dark matter density profiles for the single-population model are shown by the black solid curves in Figure 8, which we will discuss slightly later

Object	ρ_s[$M_\odot$ pc^{-3}]	r_s[kpc]	γ	i[deg]	λ	κ
Draco	$0.033^{+0.176}_{-0.028}$	$2.12^{+3.87}_{-1.35}$	$0.82^{+0.36}_{-0.42}$	77^{+9}_{-10}	$0.65^{+0.19}_{-0.17}$	$0.43^{+0.21}_{-0.15}$
Sextans	$0.016^{+0.010}_{-0.008}$	$6.22^{+2.50}_{-2.64}$	$0.29^{+0.23}_{-0.13}$	64^{+14}_{-8}	$0.71^{+0.33}_{-0.22}$	$0.38^{+0.19}_{-0.16}$
UMi	$0.023^{+0.022}_{-0.013}$	$4.70^{+3.17}_{-2.32}$	$0.35^{+0.24}_{-0.17}$	82^{+5}_{-7}	$1.32^{+0.19}_{-0.15}$	$-0.15^{+0.11}_{-0.12}$

Table 4. Best constrained model parameters based on the single-population model of three dSphs. The best-fit values are the medians of MCMC post-burn distributions, and errors are the 16th and 84th percentiles. The meanings of different model parameters can be found in Section 3.

in Section 4.2 below, together with the chemodynamical model.

In Figure 7, the observed and best-fit first (mean velocity) and second (velocity dispersion) velocity moments are shown for the three dSphs. The mean velocity and velocity dispersion profiles are calculated from the LOSVs along z'. In general, the velocity moments predicted by the best models are consistent with data, with the velocity dispersion profiles show good matches in amplitudes. The model can also recover the general shapes in the velocity dispersion profiles. In the velocity dispersion profile along the major axis of Draco and Sextans (second panels from the left in the top and middle rows), however, a few green dots drop below the model curves at $R' \sim 10 - 20$ arcmin. This is likely driven by the outer most green dots, that causes the model to match the velocity dispersion in the very outer region, sacrificing the match at $R' \sim 10 - 20$ arcmin.

For all three dSphs, rotations around major axes (green dots in the leftmost panels) are present and can be produced by the model (yellow curves). However, the matches between the black stars and the model predicted black curves (along minor axis) are poor. For axisymmetric model, the rotation is expected to be revealed in the LOSVs along the projected major axis, and this is the reason why the model can only predict a flat black curve in right-center panels along the minor axis. The deviations of black stars from zero may reflect the misalignment between minor and rotation axes in the real systems, which indicates these systems are deviating from axis-symmetry, as have been seen in simulated dSphs (Kowalczyk et al. 2018).

4.2. *Best constraints and performance of the chemodynamical model*

The full list of best-fit parameters for the chemodynamical model and for the three dSphs is provided in Table 5. Again we note large uncertainties in the inclination angle, i. Moreover, for the fractions h_1 and h_2 of metal-poor stars in red and blue templates (see Equation 13), they are close to 0 and 1, respectively. This shows that our template maps, though created through simpler hard cuts in stellar metallicities, lead to similar divisions in the stellar populations as the soft divisions according to posterior distributions of the best constrained model, which takes into account the joint spatial, kinematical and metallicity probabilities.

We also present the best constrained model parameters for the chemodynamical model by green symbols in Figure 5. The best-fit model parameters for the single-population and chemodynamical models are consistent with each other within the errors. For the tracer parameters (λ and κ), constraints of two populations in the chemodynamical model feature larger errorbars than those of the single-population model. This is because the sample size of each population is smaller than that of the total sample.

We show the best constrained dark matter density profiles through both single-population (black) and chemodynamical (orange) models in Figure 8. Given the consistency in the best constrained model parameters in Figure 5, the best-fit dark matter density profiles by the two models are also fully consistent with each other. Dark matter density profiles are best constrained around the half-number radii of tracer populations (dashed vertical lines), in that the associated statistical errors indicated by the shaded regions are smallest. This agrees with the consensus that dynamical modeling generally imposes strongest constraints on the total mass enclosed in the half-number radius of tracers (e.g. Wolf et al. 2010; Walker & Peñarrubia 2011; Wang et al. 2015; Han et al. 2016a,b; Genina et al. 2020; Wang et al. 2022; Li et al. 2022; Shi et al. 2024).

According to Figure 8, it can be seen that the half-number radii of the metal-rich and metal-poor populations sit on either sides of the half-number radii of the total population, with the metal-rich population having smaller half-number radii, but the difference is not very large. In principle, chemodynamical modeling with two distinct populations is expected to have tighter constraints at two different half-number radii of the two underlying populations, hence leads to better constraints, but Figure 8 shows that the best constraints from single-population and chemodynamical models in our analysis are very similar. This is perhaps due to the small difference in the half-number radii of the metal-rich and metal-poor populations.

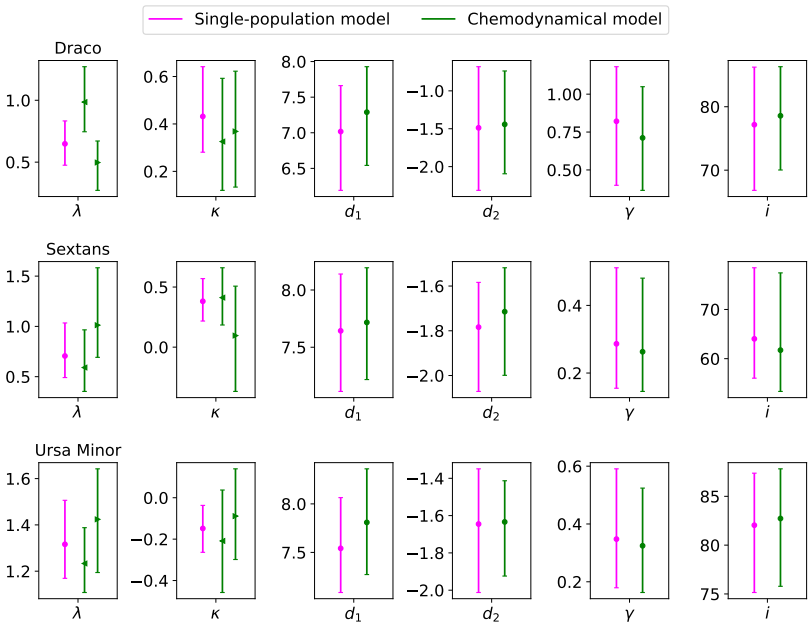

Figure 5. Best-fit model parameters for the single-population (magenta) and chemodynamical (green) models, with the three rows refer to Draco, Sextans and UMi. The left and right green arrows in the first two columns for parameters λ and κ represent results for the metal-poor and metal-rich populations separated by the chemodynamical model. The y-axis ranges for different parameters are not the same. The meanings of different model parameters can be found in Section 3.

Object	$\rho_s[\mathrm{M}_\odot\mathrm{pc}^{-3}]$	r_s[kpc]	γ	i[deg]	$\lambda^{\rm mr}$	$\lambda^{\rm mp}$	$\kappa^{\rm mr}$	$\kappa^{\rm mp}$
	$Z_0^{\rm mr}$	$Z_0^{\rm mp}$	$\sigma_Z^{\rm mr}$	$\sigma_Z^{\rm mp}$	h_1	h_2		
Draco	$0.036^{+0.147}_{-0.028}$	$2.58^{+3.52}_{-1.67}$	$0.71^{+0.34}_{-0.35}$	79^{+8}_{-9}	$0.50^{+0.17}_{-0.23}$	$0.99^{+0.29}_{-0.24}$	$0.37^{+0.25}_{-0.24}$	$0.33^{+0.27}_{-0.21}$
	$-1.75^{+0.04}_{-0.04}$	$-2.28^{+0.11}_{-0.09}$	$0.24^{+0.03}_{-0.03}$	$0.36^{+0.04}_{-0.04}$	$0.07^{+0.16}_{-0.05}$	$0.91^{+0.07}_{-0.15}$		
Sextans	$0.019^{+0.011}_{-0.009}$	$5.82^{+2.71}_{-2.39}$	$0.26^{+0.22}_{-0.12}$	62^{+12}_{-8}	$1.01^{+0.57}_{-0.32}$	$0.59^{+0.38}_{-0.24}$	$0.10^{+0.41}_{-0.46}$	$0.41^{+0.25}_{-0.23}$
	$-1.71^{+0.05}_{-0.05}$	$-2.24^{+0.05}_{-0.06}$	$0.27^{+0.04}_{-0.04}$	$0.50^{+0.03}_{-0.04}$	$0.07^{+0.09}_{-0.05}$	$0.95^{+0.04}_{-0.09}$		
UMi	$0.023^{+0.015}_{-0.011}$	$5.62^{+2.89}_{-2.53}$	$0.33^{+0.20}_{-0.16}$	83^{+5}_{-7}	$1.42^{+0.22}_{-0.23}$	$1.23^{+0.16}_{-0.13}$	$-0.09^{+0.23}_{-0.21}$	$-0.21^{+0.25}_{-0.25}$
	$-1.96^{+0.02}_{-0.02}$	$-2.32^{+0.04}_{-0.04}$	$0.26^{+0.02}_{-0.02}$	$0.50^{+0.03}_{-0.02}$	$0.03^{+0.05}_{-0.02}$	$0.89^{+0.08}_{-0.13}$		

Table 5. Best constrained model parameters for the chemodynamical model of three dSphs. The best-fit values are the medians of MCMC post-burn distributions, and errors are the 16th and 84th percentiles. The meanings of different model parameters can be found in Section 3.

Among the three dSphs, Draco has the steepest inner density profile. It favors an inner dark matter density profile $\gamma = 1$ within its 1σ confidence intervals, which is consistent with cusped NFW profile. On the other hand, dark matter halos of Sextans and UMi have lower central densities and their inner profiles are closer to cores. In our samples, the inner density slope γ of the dark matter halo features a diversity rather than a universal value. We will back discuss this point further in Section 5 below.

4.3. *Spatial, metallicity and velocity distributions of the metal-rich and metal-poor populations in the chemodynamical model*

Using Equation 17, for each star in a given dSph, we calculate the probability for it to be in the metal-rich population. Stars that have $P_i'^{\rm metal-rich} > 0.5$ and $P_i'^{\rm metal-poor} = 1 - P_i'^{\rm metal-rich} > 0.5$ are classified as members of the metal-rich population and the metal-poor population, respectively.

In Figure 9 we show the spatial, metallicity and velocity distributions of stars in metal-rich and metal-poor populations. The lack of stars at innermost radii is due to the incompleteness of our spectroscopic samples in these regions. Obviously, metal-rich populations are more concentrated in all three dSphs, while metal-poor populations tend to be more extended out to larger radii. These features are consistent with those of template maps in Figure 4. Similar findings of distinct spatial distributions of two populations in dSphs are also reported in previous works (e.g. Walker & Peñarrubia

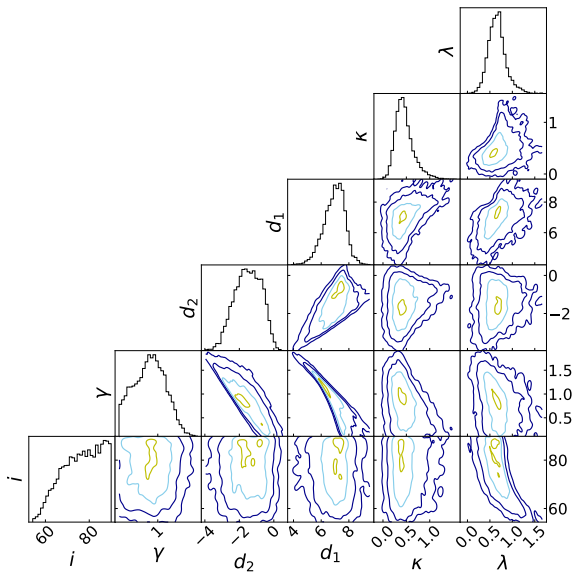

Figure 6. The likelihood contours of six model parameters for Draco. The meanings of different model parameters can be found in Section 3. The yellow, light blue and two dark blue contours represent the 10%, 1σ, 2σ and 3σ regions of the MCMC post-burn distributions, respectively.

2011; Zhu et al. 2016a; Pace et al. 2020), in that the central part of dSphs may have experienced more recent star formations, and thus the younger metal-rich population is more centrally concentrated.

The metallicity distributions show that the separation of two populations in three dSphs are mostly, but not entirely, determined by hard cuts in metallicity (gray dashed horizontal lines), as the total probability of a star within a population in Equation 16 is also contributed by the dynamical probability. There are overlaps between the metallicity distributions of the two populations, with the low metallicity tail of the metal-rich population extending lower than the hard cut, and the high metallicity tail of the metal-poor population extending higher than the hard cut. Among the three dSphs, UMi has the most dominant metal-rich population, whereas Sextans features two populations with more comparable sizes.

The two populations also differ in their global velocity distributions. Figure 10 more clearly shows the first (mean LOSV) and second (LOSV dispersion) velocity moments of the two populations, in a similar manner as Figure 7 for the single-population model, but the two stellar populations are shown in the two left (metal-poor) and two right (metal-rich) columns separately. Here we only show velocity moment profiles along major axes.

For Draco, the two populations identified by the best-fit models (symbols with error bars) show similar mean velocity profiles, which indicate rotations around the minor axes but with different amplitudes. The best-fit model predicts different signs of rotations for the two populations in Sextans, which was also seen in Sculptor (Zhu et al. 2016a). For UMi, rotation is only seen in the metal-poor population. However, the two populations show distinct velocity dispersion profiles in all three dSphs. The metal-poor populations are usually kinematically hotter, with negative gradients in their dispersion profiles that decrease with radius. On the other hand, velocity dispersion profiles of the metal-rich populations are kinematically colder and nearly flat, only slightly declining in outer regions for Sextans and UMi. These distinct properties of velocity dispersions of two populations are also consistent with those reported in previous studies (e.g. Pace et al. 2020), in that the younger metal-rich population may involve more later formed stars in central regions which have more coherent motions, hence the velocity dispersions are decreased. On the other hand, the older metal-poor population is more relaxed.

In general, the predicted mean velocity profiles by the best constrained model agree well with the data. Unfortunately, the velocity dispersion profiles are poorly fit for the metal-poor population of Draco, both populations of Sextans and the metal-poor population of UMi. These poor fittings are mainly caused by the relatively large difference between the velocity dispersions of the two populations. For all three dSphs, the central velocity dispersions of the metal-poor populations are nearly a factor of two larger than those of the metal-rich populations. If different populations have different velocity anisotropy parameters, λ, it may cause some differences in the velocity dispersion for the LOSV component. But as we have tested different values of λ to predict the velocity dispersions using Jeans equations, the difference is difficult to be as large as a factor of two. Moreover, the significantly higher velocity dispersion in metal-poor populations cannot be due to the contamination by RR Lyrae stars either, as we have excluded the entire horizontal branch (see Section 2). Moreover, we have tried to exclude a few stars with large LOSV variations based on their multi-epoch observations, which are more likely binaries, but the velocity dispersions almost do not change. We have also checked that the different LOSV dispersions of the two populations cannot be due to their different LOSV errors either.

The nearly factor of two difference in the velocity dispersions of the metal-rich and metal-poor populations may reflect that the dSph system is deviating from

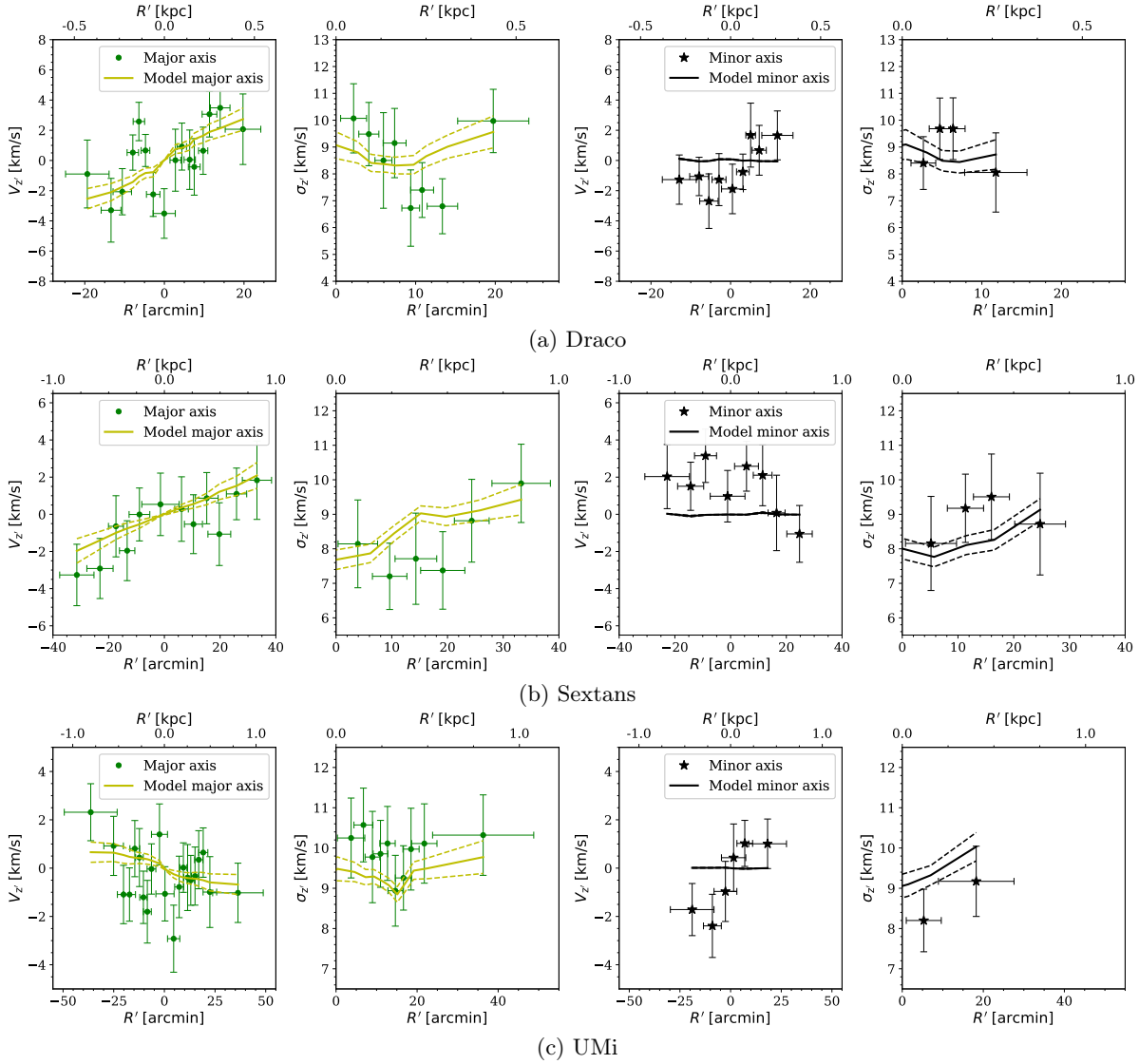

Figure 7. The mean LOSV ($v_{z'}$) and the LOSV dispersion ($\sigma_{z'}$) profiles along major (two left columns) and minor (two right columns) axes of three dSphs: (a) Draco, (b) Sextans and (c) UMi. The green dots and black stars represent the binned data within sectors of $\pm 45^{\circ}$ relative to the corresponding axes. The number of stars in each bin is the same for a given galaxy, but varies between different systems. The x errors represent the bin width while the y errors represent the 1σ scatters. The yellow and black curves represent best-fit model profiles along the projected major and minor axes, respectively. Solid and dashed curves represent best-fit model profiles and corresponding 1σ uncertainties. The velocity dispersions of both the data and the best-fit model include observational uncertainties. They are not intrinsic velocity dispersions deconvolved with errors.

the steady-state assumption behind the Jeans equations. On the other hand, for multiple tracer populations bound together and moving in the same potential, if all tracers are in steady state, we do not expect such prominent differences in their velocity dispersions. Thus the solutions to Jeans equations under the steady-state tracer assumptions are impossible to reproduce such a prominent difference between different stellar populations moving in the same potential. Hence impossible to simultaneously achieve ideal fits in the observed velocity dispersion profiles of both populations.

In particular, for Draco and UMi, the metal-rich populations in the rightmost panels dominate in sample size (see Figure 9 above), and thus the models tend to match better the metal-rich population. For Sextans, the metal-rich and metal-poor populations are more comparable in sample size, and the best-fit model tends to reconcile the large difference in velocity dispersion profiles of two populations, resulting in over-estimated dispersions for the metal-rich population, and under-estimated dispersions for the metal-poor population.

4.4. *Astrophysical factors*

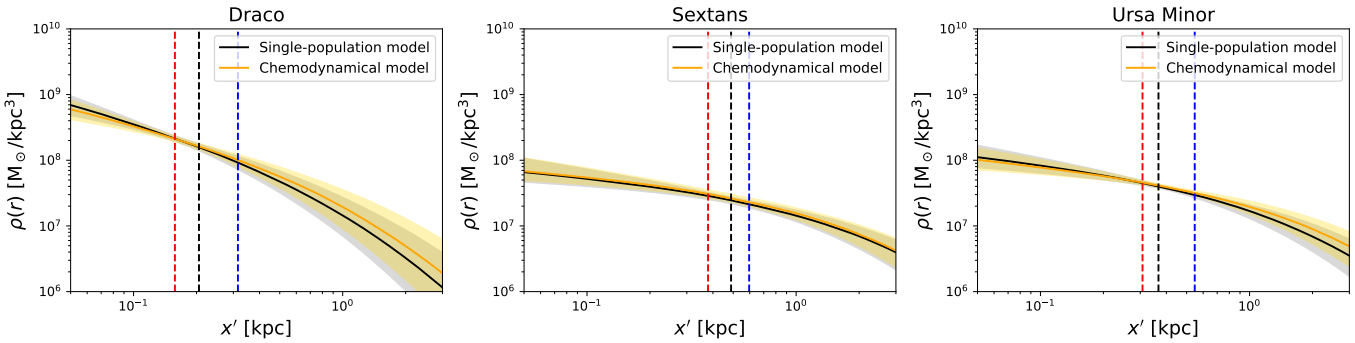

Figure 8. Best recovered dark matter density profiles of three dSphs: (a) Draco, (b) Sextans and (c) UMi. The black and orange solid lines represent median values obtained through our single-population and chemodynamical models, respectively, with shaded regions denoting the 1σ confidence regions. The black, red, and blue dashed vertical lines correspond to the half-number radii of the total, metal-rich, and metal-poor populations in each galaxy. Note that the half-number radii for the metal-rich and metal-poor populations are based on the joint posterior probability of the best model.

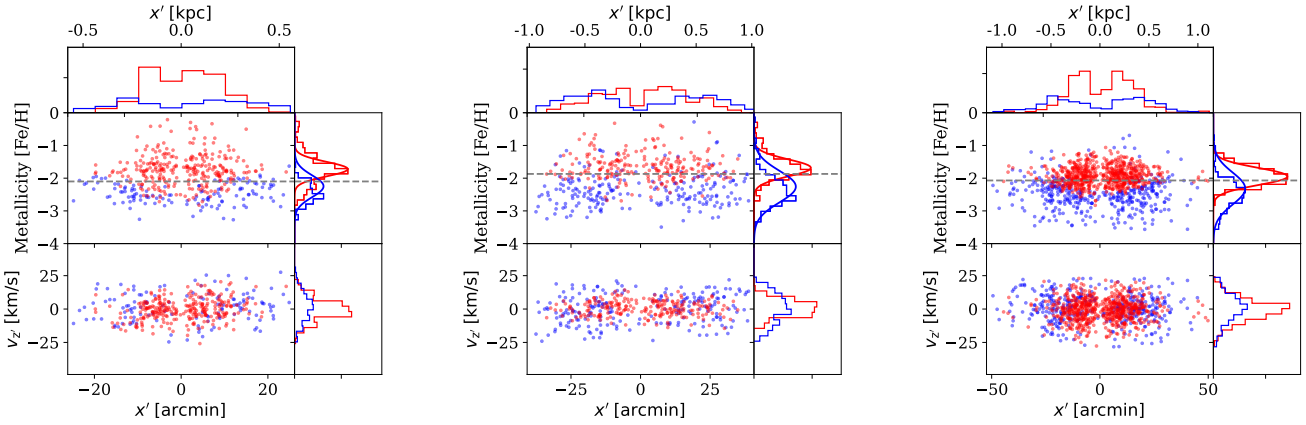

(a) Draco (b) Sextans (c) UMi

Figure 9. The spatial, metallicity and velocity distributions for the metal-rich (red points/histograms) and metal-poor (blue points/histograms) populations in three dSphs recovered by the chemodynamical model. Each sub plot has five panels. **Top histogram:** the spatial distributions of two populations. **Middle-left scatter panel:** [Fe/H] versus the projected semimajor radius x'. **Middle-right histogram:** metallicity distributions of two populations. **Bottom-left scatter panel:** the LOSV (v'_z) of each star, versus the projected semimajor radius x'. **Bottom-right histogram:** the global velocity distributions of two populations. The division of the two populations are based on the posterior probability of our best-fit model (see Equation 17), with metal-rich and metal-poor populations have this probability greater than 0.5 ($P_i'^{\rm metal-rich} > 0.5$). In the two right panels showing the histogram distributions, histograms are based on the data, while solid smooth curves with the same colors are model predictions. Grey dashed horizontal lines in middle panels denote the hard cuts in metallicity to create the red and blue spatial templates.

In this subsection, we provide our measurements of the astrophysical factors of Draco, Sextans and UMi, for the purposes of future dark matter indirect detections (e.g. Baltz et al. 1999; Bergström & Hooper 2006; Geringer-Sameth et al. 2015; Hayashi et al. 2016). The astrophysical factor is determined by the dark matter distribution within the galaxy. For dark matter annihilation or decay, the astrophysical factor is called the J or D factor, respectively. The J and D factors can be written as

$$J = \iint \rho^2_{\rm DM}(l,\Omega)\, dl d\Omega \tag{20}$$

$$, D = \iint \rho_{\rm DM}(l,\Omega)\, dl d\Omega, \tag{21}$$

where $\rho_{\rm DM}$ is the dark matter density, l is the distance along the line-of-sight direction, and Ω is the solid angle centered on the dSph.

The J and D factors of the three dSphs are provided in Table 6, with integrals in Equation 21 over a fixed solid angle of $\Delta\Omega = 0.5°$. In Figures 11 and 12, J and D fac-

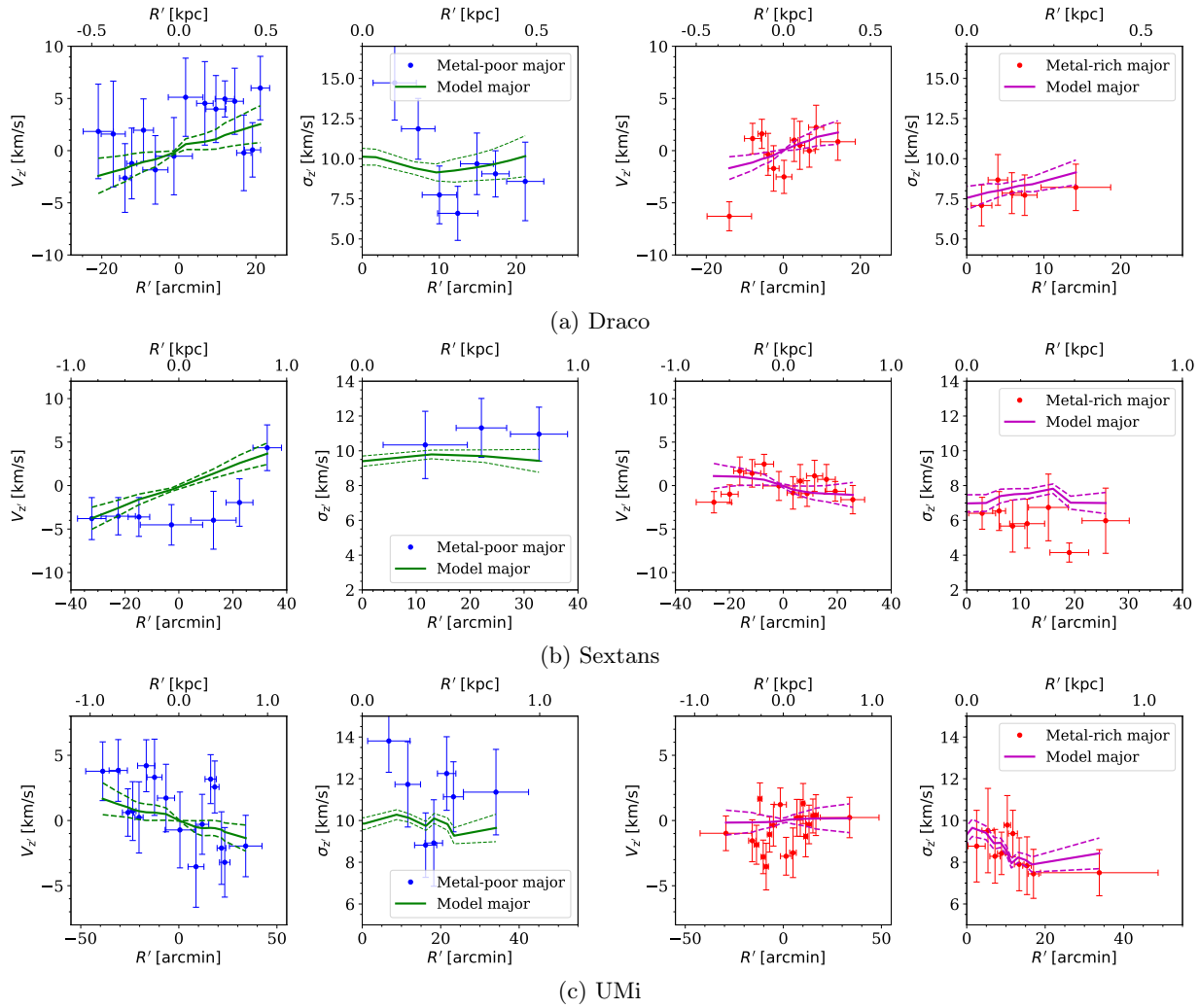

Figure 10. As Figure 7, but only for velocity moment profiles along major axes of different stellar populations in three dSphs. Two left and two right columns are the mean LOSV and LOSV dispersion profiles binned along the major axis for the metal-poor (blue dots) and metal-rich (red dots) populations, respectively. We do not show results along the minor axis, as the main trends and comparisons are very similar. In each panel, green and magenta solid curves are the best model predictions (see the legend), with the two dashed curves on both sides showing the 1-σ confidence regions. The number of stars in each bin is the same for a given population in one galaxy, but varies between populations and among dSphs.

Object	$\log_{10} J(0.5^\circ)$ $[\mathrm{GeV^2\,cm^{-5}}]$	$\log_{10} D(0.5^\circ)$ $[\mathrm{GeV\,cm^{-2}}]$
Draco	$18.74^{+0.12}_{-0.09}$	$18.07^{+0.10}_{-0.10}$
Sextans	$17.98^{+0.12}_{-0.12}$	$18.03^{+0.07}_{-0.06}$
UMi	$18.27^{+0.07}_{-0.07}$	$18.20^{+0.04}_{-0.05}$

Table 6. Values of J and D factors for three dSphs within 0.5°.

tors calculated from Hayashi et al. (2020) and this work are compared. The differences are mainly due to different dark matter halo models adopted and different truncation radii of dark matter halos. Hayashi et al. (2020) assumed axisymmetric dark matter halos with generalized Hernquist profiles (Hernquist 1990; Zhao 1996), while in our analysis we consider spherical dark matter halos with generalized NFW profiles, and the outer density slope has been fixed to 4. On the other hand, both Hayashi et al. (2020) and us truncate the dark matter halo at the projected radius of the outermost observed member star for each dSphs. However, stars beyond 2.5 half-light radius from the center of each dSphs are not used in our analysis (see Section 2.4), and thus the truncation radius for the dark matter halo in our analysis, i.e., 2.5 half-light radius, is smaller than that of Hayashi et al. (2020). In Figures 11 and 12, the most prominent difference between Hayashi et al. (2020) and this work is the D factor for Draco. This is because their truncation radius for Draco is much larger than ours and the dark matter distribution at larger radii contributes

more to the D factor than the J factor. Besides, since we truncate dark matter halos at smaller radii where dark matter density profiles are better constrained, uncertainties of our J and D factors are also reduced. In our results, Draco turns out to be the most promising target to search for signals of dark matter annihilation and decay.

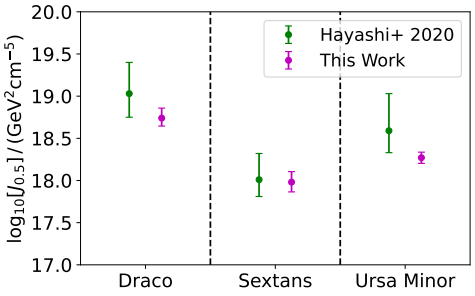

Figure 11. Measured J factors for three dSphs. Green and magenta symbols denote those of Hayashi et al. (2020) and this work.

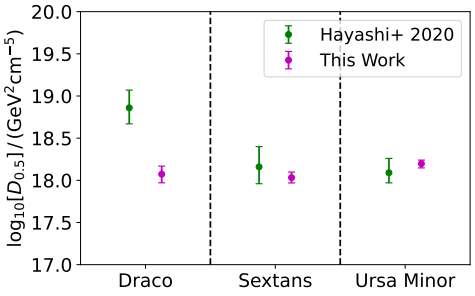

Figure 12. Measured D factors for three dSphs. Green and magenta symbols denote those of Hayashi et al. (2020) and this work.

5. DISCUSSIONS

In Read et al. (2019), the dark matter density at 150 pc, $\rho_{\rm DM}(150{\rm pc})$, is used as a proxy of the inner density slope γ. We compare our results of $\rho_{\rm DM}(150{\rm pc})$ with those reported by Read et al. (2019) and Hayashi et al. (2020) in Figure 13. For the three dSphs used in our analysis, we mark our best recovered $\rho_{\rm DM}(150{\rm pc})$ from the chemodynamical model above by the magenta filled circles, and we do not repeatedly show those for the single-population model as they are very similar (see Figure 8). Previous measurements by Read et al. (2019) and Hayashi et al. (2020) are plotted with black stars and green diamonds.

For Draco, our measured $\rho_{\rm DM}(150{\rm pc})$ agrees well with both Read et al. (2019) and Hayashi et al. (2020). For Sextans, three measurements are different from each

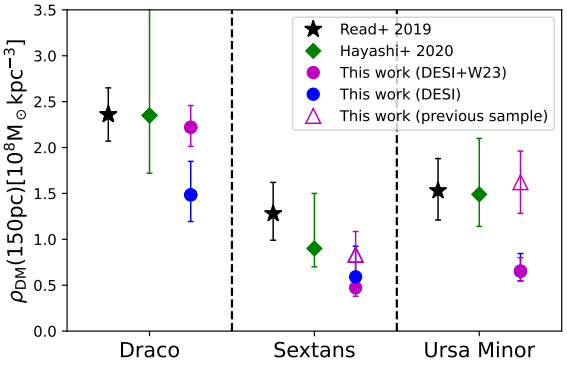

Figure 13. The dark matter densities at 150pc for the three dSphs. The black stars and green diamonds represent results in Read et al. (2019) and Hayashi et al. (2020). The magenta filled circles represent our results using the combined member star sample from DESI observation and Walker et al. (2023), based on the best constrained chemodynamical model. Results of the single-population model are very similar (see Figure 8), and thus are not shown. Blue filled circles are measurements based on DESI observed member stars only. For UMi the magenta filled circle overlaps the blue filled circle. We also repeat our analysis for Sextans and UMi using the same member star samples as Hayashi et al. (2020), and show the results by hollow magenta triangles.

other, though the measurements of Hayashi et al. (2020) and Read et al. (2019) still agree within the errors. This discrepancy is very likely due to the fact that both Hayashi et al. (2020) and us adopt axisymmetric Jeans analysis, while Read et al. (2019) used spherical Jeans models. Thus our measurement and the measurement by Hayashi et al. (2020) for Sextans are both lower than that of Read et al. (2019). Besides, the sample of member stars used in Hayashi et al. (2020) is different from that in this work. We have carefully repeated our calculation by using the same sample as in Hayashi et al. (2020), and we can reproduce the result of Hayashi et al. (2020) for Sextans, as shown by the hollow magenta triangle in Figure 13. For UMi, our result is inconsistent with both Read et al. (2019) and Hayashi et al. (2020), and the difference is larger than that for Sextans. We have explicitly checked that this disagreement is mainly due to the large difference in the sample of member stars used for UMi, as the member star sample with LOSV measurements in our analysis is three times larger than those in Hayashi et al. (2020) or Read et al. (2019). We have also repeated our analysis by using the same sample of UMi as in Hayashi et al. (2020), and we again obtain consistent result with both Read et al. (2019) and Hayashi et al. (2020), with the best constraint shown by the hollow magenta triangle in Figure 13. This test robustly confirms that it is mainly the difference in the sample of member stars used in different analysis that

leads to the discrepancy between our measurement and those in the two previous studies for UMi.

We have checked that the intrinsic velocity dispersion profiles for the member star sample of Hayashi et al. (2020) and of our analysis above (DESI + Walker et al. (2023)) differ for both Sextans and UMi, and in turn significantly influence the inferred dark matter content. Here the intrinsic velocity dispersions deconvolved from observational errors are calculated following the method[7] in Li et al. (2017), and we have corrected LOSV offsets between the two data samples. We find that the sample in Hayashi et al. (2020) has higher intrinsic velocity dispersions in the central region than our sample, and this is the reason for the lower density $\rho_{\rm DM}(150{\rm pc})$ obtained in our analysis. In fact, the member stars of UMi in Hayashi et al. (2020) are more metal-poor than our sample, which results in higher velocity dispersion in the center. However, given the significantly increased number of DESI observed member stars for UMi, we believe our sample is more complete.

The different intrinsic velocity dispersions are due to the difference in the selection functions of these observations. Throughout this paper, we have been assuming that the fiber assignment does not depend on velocity, and the velocity dispersion profiles of observed member stars in the three dSphs do not differ from those of targets. However, based on our discussion above, this assumption does not hold for all observations, i.e., the sample of stars used in Hayashi et al. (2020) is more metal-poor than ours.

Since different samples may subject to different selection functions that can affect the velocity dispersion profiles, the combination of two data sets in this work, i.e., data from DESI and Walker et al. (2023), may also introduce complicated selection effects. Thus we perform further checks. For each dSph, we first calculate the intrinsic velocity dispersions for the same sample of stars existing in both DESI and Walker et al. (2023). The intrinsic velocity dispersions computed using LOSV measurements from both fully agree with each other, indicating the measurements of LOSV and associated uncertainties are reliable in both DESI and Walker et al. (2023). However, if we use all member stars either in DESI or Walker et al. (2023), after correcting for the mean offset between LOSVs in the two data sets, the resulting intrinsic velocity dispersion profiles based on the data set of Walker et al. (2023) are slightly different from those of DESI observed member stars for Draco and Sextans, while there is no difference for UMi. The agreement between DESI and Walker et al. (2023) UMi sample is reassuring, indicating that the large sample of DESI observed UMi member stars is unlikely subject to strong selection biases.

Given the difference in the intrinsic velocity dispersions based on DESI and Walker et al. (2023) member stars for Draco and Sextans, we repeat our modeling using only DESI data for them. We show the dark matter density profiles in Figure 15 of Appendix A. For Draco and Sextans, indeed the best constrained dark matter density profiles differ when we use only DESI observed member stars, and when using the combined sample of DESI + Walker et al. (2023). Nevertheless, the differences are still marginally consistent within the large 1-σ errors.

The best recovered $\rho_{\rm DM}(150{\rm pc})$ of three dSphs using only DESI data are shown by the blue filled circles in Figure 13. The intrinsic velocity dispersions of Sextans/Draco, if only using DESI observed stars, are higher/lower in the central region than using the combined data, hence resulting in higher/lower $\rho_{\rm DM}(150{\rm pc})$. For Sextans, since the difference between the blue and magenta circles of Sextans is less significant compared with the errorbars, we think selection effects associated with Sextans are not strong enough to violate the conclusion. For Draco, DESI is missing a lot of metal-poor stars in the central region, which is at least partially because the number of observed member stars in DESI is small (less than 100, see Table 2). On the other hand, Walker et al. (2023) observes more member stars in the center of Draco. Hence the best constrained $\rho_{\rm DM}(150{\rm pc})$ for Draco is more robust with the combined data set of DESI + Walker et al. (2023), i.e., the magenta circle in Figure 13.

Finally, we show in Figure 14 the best recovered $\rho_{\rm DM}(150{\rm pc})$ for dwarf galaxies in Read et al. (2019) and Hayashi et al. (2020), in addition to the three dSphs in our analysis. A few dwarf irregular galaxies used by Read et al. (2019) are marked with black squares. The values of $M_\star/M_{200}$ (the x-axis) for all dSphs are just taken from Read et al. (2019), which are obtained through abundance matching. We do not calculate them again. Read et al. (2019) reached a very important conclusion that there is a negative correlation between $\rho_{\rm DM}(150{\rm pc})$ and $M_\star/M_{200}$, which supports stellar feedback as the scenario to explain the core-cusp problem for dwarf galaxies. However, similar trend is not clearly seen

[7] They use a two-parameter Gaussian likelihood function similar to that of Walker et al. (2006) to calculate the systemic velocity and the intrinsic velocity dispersion of a sample of stars: $\log\mathcal{L} = -\frac{1}{2}\left[\sum\log(\sigma^2_{v_{\rm sys}}+\sigma^2_{v_i}) + \sum(v_i - v_{\rm sys})^2/(\sigma^2_{v_i}+\sigma^2_{v_{\rm sys}})\right]$, where $v_{\rm sys}$ and $\sigma_{v_{\rm sys}}$ are the systemic velocity and the intrinsic velocity dispersion of the sample, and v_i and σ_{v_i} are the velocity and the velocity uncertainty of each star.

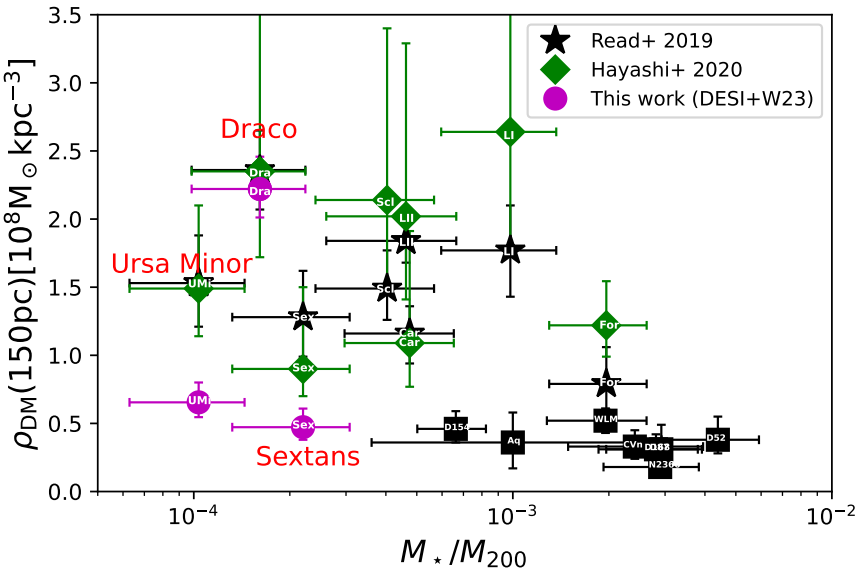

Figure 14. The dark matter densities at 150pc (y-axis) versus the stellar-to-halo mass ratios (x-axis) for dwarf galaxies in a few previous studies. The black filled squares and stars denote results in Read et al. (2019) for dwarf irregular galaxies (dIrrs) and dwarf spheroidal galaxies (dSphs), respectively. The green symbols represent results in Hayashi et al. (2020). The magenta filled circles represent results in our main analysis using the combined member star sample from DESI observation and Walker et al. (2023), based on the best constrained chemodynamical model in this work.

in Hayashi et al. (2020), due to the fact that Hayashi et al. (2020) did not include those dwarf Irregulars used in Read et al. (2019), and the measured inner densities for Fornax and LeoI on the right side of Figure 14 are higher than those by Read et al. (2019). Our results, denoted by filled magenta circles in Figure 14, do not fully follow this anti-correlation due to the lower values of $\rho_{\rm DM}(150{\rm pc})$ of Sextans and UMi.

Even with only three dSphs, we find a diversity of $\rho_{\rm DM}(150{\rm pc})$, or the inner density slope, γ, with $\rho_{\rm DM}(150{\rm pc})$ spanning one order of magnitude for the three dSphs. Draco has the highest density $\rho_{\rm DM}(150{\rm pc})$ with the inner density slope $\gamma = 0.71^{+0.34}_{-0.35}$ close to 1, while dark halos of Sextans and UMi are less dense in inner regions with smaller γ, $0.26^{+0.22}_{-0.12}$ and $0.33^{+0.20}_{-0.16}$, which are closer to cored models. Moreover, by comparing the measured inner densities for the three dSphs used in our analysis with Read et al. (2019) and Hayashi et al. (2020), and by repeating our analysis using member stars observed in different surveys, we have demonstrated that the currently best constrained inner density slopes are still sensitive to the model assumptions and to sample selection effects.

6. CONCLUSIONS

Three classical dSphs (Draco, Sextans and UMi) have been observed by DESI MWS so far. We combine the line-of-sight velocity and metallicity measurements from DESI MWS with those in Walker et al. (2023) to construct the so-far largest member star samples with spectroscopic observations of the three dSphs. To recover their inner dark matter distributions, the axisymmetric Jeans Anisotropic Multi-Gaussian Expansion modeling (JAM) approach is adopted. In particular, we use both traditional single-population Jeans modeling and multiple population chemodynamical modeling for our analysis.

We find the best recovered model parameters and the underlying dark matter radial density profiles are consistent between single-population and chemodynamical models. The dark matter density profiles are best constrained around the half-number radii of tracer member stars. A diversity is found for the inner density slopes γ of host dark matter halos for the three dSphs. The inner density slopes are $0.71^{+0.34}_{-0.35}$, $0.26^{+0.22}_{-0.12}$ and $0.33^{+0.20}_{-0.16}$ for Draco, Sextans and UMi, respectively.

With the chemodynamical model, member stars with spectroscopic observations of each dSph are divided into metal-rich and metal-poor populations, based on their chemical, spatial and dynamical properties. The metal-rich populations are more centrally concentrated, while the metal-poor populations are more extended. Rotations around minor axes are found for both populations. Moreover, the metal-rich populations are dynamically colder, featuring lower velocity dispersion profiles than the metal-poor populations in all three dSphs.

We compare our results with those in two important previous studies, Read et al. (2019) and Hayashi et al.

(2020). Our measurement for Draco agrees well with both of Read et al. (2019) and Hayashi et al. (2020). For Sextans, all three measurements are different from each other. This discrepancy is mainly because both Hayashi et al. (2020) and us adopt axisymmetric Jeans analysis, whereas the model of Read et al. (2019) is based on spherical Jeans modeling. Besides, the sample of member stars used by Hayashi et al. (2020) has higher velocity dispersion in the center, resulting in higher dark matter density. Our best recovered $\rho_{\rm DM}(150)$ of UMi is much lower than both Read et al. (2019) and Hayashi et al. (2020), which is because the UMi member stars in Read et al. (2019) and Hayashi et al. (2020) are more metal-poor and have higher velocity dispersion in the center than ours. Since the member star sample observed by DESI is significantly larger than those in previous observations, especially for UMi, we believe our sample subjects less to selection effects.

In addition to UMi, we also see possible sample selection effects for Draco and Sextans, i.e., their intrinsic velocity dispersions based on the sample of member stars in Walker et al. (2023) are different from those based on only DESI observed member stars. We thus compare the best constraints of using only DESI member stars with the DESI + Walker et al. (2023) data. For Sextans, the best constrained $\rho_{\rm DM}(150{\rm pc})$ by using DESI data is slightly higher than that of using the combined data set, but the difference is less significant compared with errors. For Draco, if only using DESI observed member stars, we find $\rho_{\rm DM}(150{\rm pc})$ becomes significantly lower than that of using DESI + Walker et al. (2023) data, mainly due to the the lacking of DESI observed metal-poor member stars in central regions.

In particular, Read et al. (2019) finds an anti-correlation between the inner dark matter densities and the stellar-to-halo mass ratios for dSphs, which supports the stellar feedback scenario to explain the core-cusp problem. The measurements by Hayashi et al. (2020) and in our current analysis do not fully track the anti-correlation reported by Read et al. (2019) at the low value end of M_*/M_{200}. Our results indicate that the study of the dark matter content of dSphs through stellar kinematics is still subject to uncertainties in both the model assumption and selection effects in the observed data.

We also estimate astrophysical J and D factors of the three dSphs. Draco has the largest J or D factors, which makes it the most promising target for searches of dark matter annihilation and decay signals.

The data used for all figures in this work can be found at https://zenodo.org/records/15723563.

ACKNOWLEDGMENTS

This work is supported by NSFC (12273021,12022307) and the National Key R&D Program of China (2023YFA1605600, 2023YFA1605601, 2023YFA1607800, 2023YFA1607801), 111 project (No. B20019), and the science research grants from the China Manned Space Project (No. CMS-CSST-2021-A03). We thank the sponsorship from Yangyang Development Fund. The computations of this work are carried on the Gravity supercomputer at the Department of Astronomy, Shanghai Jiao Tong University and the National Energy Research Scientific Computing Center (NERSC). HY is supported by T.D. Lee scholarship. LZ acknowledges the support from CAS Project for Young Scientists in Basic Research, Grant No. YSBR-062. SK acknowledges support from the Science & Technology Facilities Council (STFC) grant ST/Y001001/1.

We are grateful for helps by Kohei Hayashi, who has kindly shared with us the member star catalog. We also thank our DESI publication handler, Ting Tan, for his helps and coordinations.

This material is based upon work supported by the U.S. Department of Energy (DOE), Office of Science, Office of High-Energy Physics, under Contract No. DE–AC02–05CH11231, and by the National Energy Research Scientific Computing Center, a DOE Office of Science User Facility under the same contract. Additional support for DESI was provided by the U.S. National Science Foundation (NSF), Division of Astronomical Sciences under Contract No. AST-0950945 to the NSF's National Optical-Infrared Astronomy Research Laboratory; the Science and Technology Facilities Council of the United Kingdom; the Gordon and Betty Moore Foundation; the Heising-Simons Foundation; the French Alternative Energies and Atomic Energy Commission (CEA); the National Council of Humanities, Science and Technology of Mexico (CONAHCYT); the Ministry of Science, Innovation and Universities of Spain (MICIU/AEI/10.13039/501100011033), and by the DESI Member Institutions: https://www.desi.lbl.gov/collaborating-institutions. Any opinions, findings, and conclusions or recommendations expressed in this material are those of the author(s) and do not necessarily reflect the views of the U. S. National Science Foundation, the U. S. Department of Energy, or any of the listed funding agencies.

The authors are honored to be permitted to conduct scientific research on I'oligam Du'ag (Kitt Peak), a mountain with particular significance to the Tohono O'odham Nation.

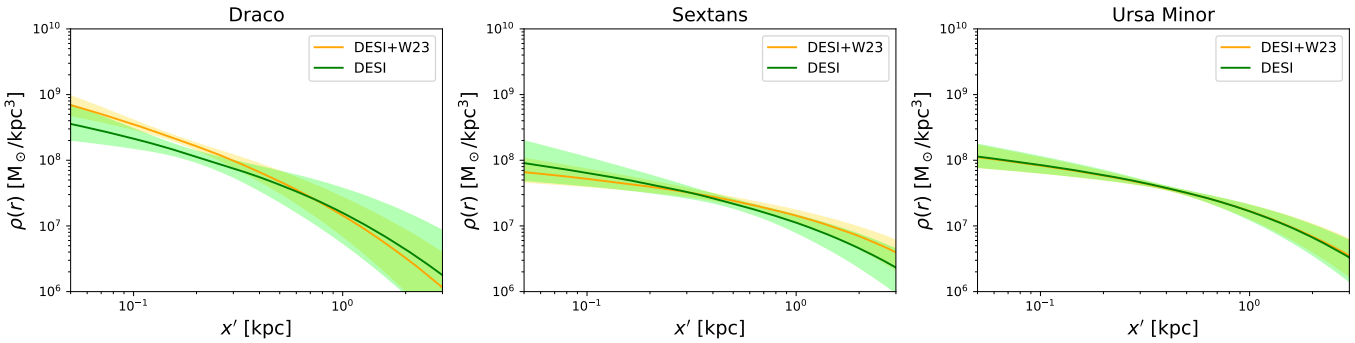

Figure 15. As Figure 8, but for best constrained dark matter density profiles based on the combined data (DESI + Walker et al. (2023)) and only DESI data. All constraints in this figure are from the single population model, with the chemodynamical model leads to very similar results and are thus not repeatedly shown. The orange curves represents the best constrained dark matter density profiles of the combined data, which is exactly the same as the black solid curves in Figure 8 of the main text. The green curves represents those using only DESI observed member stars. The shaded region with corresponding colors show the associated 1-σ uncertainties.

any Author Accepted Manuscript version arising from this submission.

APPENDIX

A. INVESTIGATIONS ON SAMPLE SELECTION EFFECT

In the main text we present results based on the combined member star sample by DESI and in Walker et al. (2023). To check sample selection effects, we repeat our analysis using only DESI observed member stars. In Figure 15 we show the best constrained dark matter density profiles of the combined data (orange) and DESI data (green). For Draco, the dark matter density profile is much lower in inner regions if only using DESI data. This is mainly because DESI observes a small number of stars in Draco (less than 100), and the sample of Walker et al. (2023) has more metal-poor stars observed in the center, featuring higher central velocity dispersions. For Sextans, the dark matter density profile if only using DESI data is slightly higher in the central region due to its higher velocity dispersion profile. For UMi, there is no significant difference between inner density profiles of the combined data and DESI data.

REFERENCES

Adame, A. G., Aguilar, J., Ahlen, S., et al. 2025a, JCAP, 2025, 124, doi: 10.1088/1475-7516/2025/01/124

—. 2025b, JCAP, 2025, 021, doi: 10.1088/1475-7516/2025/02/021

Agnello, A., & Evans, N. W. 2012, ApJL, 754, L39, doi: 10.1088/2041-8205/754/2/L39

Amorisco, N. C., Agnello, A., & Evans, N. W. 2013, MNRAS, 429, L89, doi: 10.1093/mnrasl/sls031

Amorisco, N. C., & Evans, N. W. 2012a, ApJL, 756, L2, doi: 10.1088/2041-8205/756/1/L2

—. 2012b, MNRAS, 419, 184, doi: 10.1111/j.1365-2966.2011.19684.x

Arroyo-Polonio, J. M., Battaglia, G., Thomas, G. F., et al. 2024, A&A, 692, A195, doi: 10.1051/0004-6361/202451102

Baltz, E. A., Briot, C., Salati, P., Taillet, R., & Silk, J. 1999, PhRvD, 61, 023514, doi: 10.1103/PhysRevD.61.023514

Battaglia, G., Helmi, A., Tolstoy, E., et al. 2008, ApJL, 681, L13, doi: 10.1086/590179

Bergström, L., & Hooper, D. 2006, PhRvD, 73, 063510, doi: 10.1103/PhysRevD.73.063510

Boldrini, P. 2021, Galaxies, 10, 5, doi: 10.3390/galaxies10010005

Bressan, A., Marigo, P., Girardi, L., et al. 2012, MNRAS, 427, 127, doi: 10.1111/j.1365-2966.2012.21948.x

Bullock, J. S., & Boylan-Kolchin, M. 2017, ARA&A, 55, 343, doi: 10.1146/annurev-astro-091916-055313

Burkert, A. 1995, ApJL, 447, L25, doi: 10.1086/309560

Cappellari, M. 2008, MNRAS, 390, 71, doi: 10.1111/j.1365-2966.2008.13754.x

Clementini, G., Ripepi, V., Molinaro, R., et al. 2019, A&A, 622, A60, doi: 10.1051/0004-6361/201833374
Cole, S., Percival, W. J., Peacock, J. A., et al. 2005, MNRAS, 362, 505, doi: 10.1111/j.1365-2966.2005.09318.x
Cooper, A. P., Koposov, S. E., Allende Prieto, C., et al. 2023, ApJ, 947, 37, doi: 10.3847/1538-4357/acb3c0
Dawson, K. S., Schlegel, D. J., Ahn, C. P., et al. 2013, AJ, 145, 10, doi: 10.1088/0004-6256/145/1/10
de Blok, W. J. G. 2010, Advances in Astronomy, 2010, 789293, doi: 10.1155/2010/789293
de Blok, W. J. G., McGaugh, S. S., & Rubin, V. C. 2001, AJ, 122, 2396, doi: 10.1086/323450
Deason, A. J., Bose, S., Fattahi, A., et al. 2022, MNRAS, 511, 4044, doi: 10.1093/mnras/stab3524
del Pino, A., Libralato, M., van der Marel, R. P., et al. 2022, ApJ, 933, 76, doi: 10.3847/1538-4357/ac70cf
DESI Collaboration, Abdul-Karim, M., Adame, A. G., et al. 2025a, arXiv e-prints, arXiv:2503.14745, doi: 10.48550/arXiv.2503.14745
DESI Collaboration, Abdul-Karim, M., Aguilar, J., et al. 2025b, arXiv e-prints, arXiv:2503.14738, doi: 10.48550/arXiv.2503.14738
DESI Collaboration, Aghamousa, A., Aguilar, J., et al. 2016a, arXiv e-prints, arXiv:1611.00036, doi: 10.48550/arXiv.1611.00036
—. 2016b, arXiv e-prints, arXiv:1611.00037, doi: 10.48550/arXiv.1611.00037
DESI Collaboration, Abareshi, B., Aguilar, J., et al. 2022, AJ, 164, 207, doi: 10.3847/1538-3881/ac882b
DESI Collaboration, Adame, A. G., Aguilar, J., et al. 2024a, arXiv e-prints, arXiv:2404.03000, doi: 10.48550/arXiv.2404.03000
—. 2024b, AJ, 167, 62, doi: 10.3847/1538-3881/ad0b08
—. 2024c, AJ, 168, 58, doi: 10.3847/1538-3881/ad3217
—. 2024d, arXiv e-prints, arXiv:2411.12021, doi: 10.48550/arXiv.2411.12021
—. 2024e, arXiv e-prints, arXiv:2411.12020, doi: 10.48550/arXiv.2411.12020
—. 2024f, arXiv e-prints, arXiv:2411.12022, doi: 10.48550/arXiv.2411.12022
Di Cintio, A., Brook, C. B., Macciò, A. V., et al. 2014, MNRAS, 437, 415, doi: 10.1093/mnras/stt1891
Eisenstein, D. J., Zehavi, I., Hogg, D. W., et al. 2005, ApJ, 633, 560, doi: 10.1086/466512
Feast, M. W., Thackeray, A. D., & Wesselink, A. J. 1961, MNRAS, 122, 433, doi: 10.1093/mnras/122.5.433
Flores, R. A., & Primack, J. R. 1994, ApJL, 427, L1, doi: 10.1086/187350
Foot, R., & Vagnozzi, S. 2015, PhRvD, 91, 023512, doi: 10.1103/PhysRevD.91.023512
Freundlich, J., Dekel, A., Jiang, F., et al. 2020a, MNRAS, 491, 4523, doi: 10.1093/mnras/stz3306
Freundlich, J., Jiang, F., Dekel, A., et al. 2020b, MNRAS, 499, 2912, doi: 10.1093/mnras/staa2790
Genina, A., Benítez-Llambay, A., Frenk, C. S., et al. 2018, MNRAS, 474, 1398, doi: 10.1093/mnras/stx2855
Genina, A., Read, J. I., Frenk, C. S., et al. 2020, MNRAS, 498, 144, doi: 10.1093/mnras/staa2352
Gentile, G., Salucci, P., Klein, U., Vergani, D., & Kalberla, P. 2004, MNRAS, 351, 903, doi: 10.1111/j.1365-2966.2004.07836.x
Geringer-Sameth, A., Koushiappas, S. M., & Walker, M. 2015, ApJ, 801, 74, doi: 10.1088/0004-637X/801/2/74
Gilmore, G., Wilkinson, M. I., Wyse, R. F. G., et al. 2007, ApJ, 663, 948, doi: 10.1086/518025
Han, J., Wang, W., Cole, S., & Frenk, C. S. 2016a, MNRAS, 456, 1003, doi: 10.1093/mnras/stv2707
—. 2016b, MNRAS, 456, 1017, doi: 10.1093/mnras/stv2522
Han, J., Eke, V. R., Frenk, C. S., et al. 2015, MNRAS, 446, 1356, doi: 10.1093/mnras/stu2178
Hargreaves, J. C., Gilmore, G., & Annan, J. D. 1996, MNRAS, 279, 108, doi: 10.1093/mnras/279.1.108
Hayashi, K., Chiba, M., & Ishiyama, T. 2020, ApJ, 904, 45, doi: 10.3847/1538-4357/abbe0a
Hayashi, K., Fabrizio, M., Łokas, E. L., et al. 2018, MNRAS, 481, 250, doi: 10.1093/mnras/sty2296
Hayashi, K., Ichikawa, K., Matsumoto, S., et al. 2016, MNRAS, 461, 2914, doi: 10.1093/mnras/stw1457
Henriques, B. M. B., White, S. D. M., Lemson, G., et al. 2012, MNRAS, 421, 2904, doi: 10.1111/j.1365-2966.2012.20521.x
Hernquist, L. 1990, ApJ, 356, 359, doi: 10.1086/168845
Hu, W., Barkana, R., & Gruzinov, A. 2000, PhRvL, 85, 1158, doi: 10.1103/PhysRevLett.85.1158
Hui, L., Ostriker, J. P., Tremaine, S., & Witten, E. 2017, PhRvD, 95, 043541, doi: 10.1103/PhysRevD.95.043541
Jiang, F., Benson, A., Hopkins, P. F., et al. 2023, MNRAS, 521, 4630, doi: 10.1093/mnras/stad705
Kaplinghat, M., Tulin, S., & Yu, H.-B. 2016, PhRvL, 116, 041302, doi: 10.1103/PhysRevLett.116.041302
Koposov, S. E., Allende Prieto, C., Cooper, A. P., et al. 2024, MNRAS, 533, 1012, doi: 10.1093/mnras/stae1842
Koposov, S. E., Li, T. S., Allende Prieto, C., et al. 2025, arXiv e-prints, arXiv:2505.14787, doi: 10.48550/arXiv.2505.14787
Kowalczyk, K., Łokas, E. L., & Valluri, M. 2018, MNRAS, 476, 2918, doi: 10.1093/mnras/sty436
Lazar, A., Bullock, J. S., Boylan-Kolchin, M., et al. 2020, MNRAS, 497, 2393, doi: 10.1093/mnras/staa2101

Levi, M., Bebek, C., Beers, T., et al. 2013, arXiv e-prints, arXiv:1308.0847, doi: 10.48550/arXiv.1308.0847

Li, Q., Han, J., Wang, W., et al. 2022, MNRAS, 514, 5890, doi: 10.1093/mnras/stac1739

Li, T. S., Simon, J. D., Drlica-Wagner, A., et al. 2017, ApJ, 838, 8, doi: 10.3847/1538-4357/aa6113

Li, Z., Dekel, A., Mandelker, N., Freundlich, J., & François, T. L. 2023, MNRAS, 518, 5356, doi: 10.1093/mnras/stac3233

Mashchenko, S., Wadsley, J., & Couchman, H. M. P. 2008, Science, 319, 174, doi: 10.1126/science.1148666

Medina, G. E., Li, T. S., Koposov, S. E., et al. 2025a, arXiv e-prints, arXiv:2504.02924, doi: 10.48550/arXiv.2504.02924

Medina, G. E., Li, T. S., Allende Prieto, C., et al. 2025b, arXiv e-prints, arXiv:2505.10614, doi: 10.48550/arXiv.2505.10614

Miller, T. N., Doel, P., Gutierrez, G., et al. 2024, AJ, 168, 95, doi: 10.3847/1538-3881/ad45fe

Minor, Q. E., Martinez, G., Bullock, J., Kaplinghat, M., & Trainor, R. 2010, ApJ, 721, 1142, doi: 10.1088/0004-637X/721/2/1142

Moore, B. 1994, Nature, 370, 629, doi: 10.1038/370629a0

Muñoz, R. R., Côté, P., Santana, F. A., et al. 2018, ApJ, 860, 66, doi: 10.3847/1538-4357/aac16b

Navarro, J. F., Eke, V. R., & Frenk, C. S. 1996a, MNRAS, 283, L72, doi: 10.1093/mnras/283.3.L72

Navarro, J. F., Frenk, C. S., & White, S. D. M. 1995, MNRAS, 275, 720, doi: 10.1093/mnras/275.3.720

—. 1996b, ApJ, 462, 563, doi: 10.1086/177173

—. 1997, ApJ, 490, 493, doi: 10.1086/304888

Oh, S.-H., Brook, C., Governato, F., et al. 2011, AJ, 142, 24, doi: 10.1088/0004-6256/142/1/24

Oman, K. A., Navarro, J. F., Fattahi, A., et al. 2015, MNRAS, 452, 3650, doi: 10.1093/mnras/stv1504

Pace, A. B., Erkal, D., & Li, T. S. 2022, ApJ, 940, 136, doi: 10.3847/1538-4357/ac997b

Pace, A. B., Kaplinghat, M., Kirby, E., et al. 2020, MNRAS, 495, 3022, doi: 10.1093/mnras/staa1419

Pontzen, A., & Governato, F. 2012, MNRAS, 421, 3464, doi: 10.1111/j.1365-2966.2012.20571.x

—. 2014, Nature, 506, 171, doi: 10.1038/nature12953

Poppett, C., Tyas, L., Aguilar, J., et al. 2024, AJ, 168, 245, doi: 10.3847/1538-3881/ad76a4

Read, J. I., & Gilmore, G. 2005, MNRAS, 356, 107, doi: 10.1111/j.1365-2966.2004.08424.x

Read, J. I., Walker, M. G., & Steger, P. 2019, MNRAS, 484, 1401, doi: 10.1093/mnras/sty3404

Rocha, M., Peter, A. H. G., Bullock, J. S., et al. 2013, MNRAS, 430, 81, doi: 10.1093/mnras/sts514

Schlafly, E. F., Kirkby, D., Schlegel, D. J., et al. 2023, AJ, 166, 259, doi: 10.3847/1538-3881/ad0832

Sesar, B., Hernitschek, N., Mitrović, S., et al. 2017, AJ, 153, 204, doi: 10.3847/1538-3881/aa661b

Shi, R., Wang, W., Li, Z., et al. 2024, ApJ, 973, 82, doi: 10.3847/1538-4357/ad64cf

Silber, J. H., Fagrelius, P., Fanning, K., et al. 2023, AJ, 165, 9, doi: 10.3847/1538-3881/ac9ab1

Spencer, M. E., Mateo, M., Walker, M. G., et al. 2017, AJ, 153, 254, doi: 10.3847/1538-3881/aa6d51

Spergel, D. N., & Steinhardt, P. J. 2000, PhRvL, 84, 3760, doi: 10.1103/PhysRevLett.84.3760

Springel, V., Pakmor, R., Pillepich, A., et al. 2018, MNRAS, 475, 676, doi: 10.1093/mnras/stx3304

Strigari, L. E., Frenk, C. S., & White, S. D. M. 2017, ApJ, 838, 123, doi: 10.3847/1538-4357/aa5c8e

Tollet, E., Macciò, A. V., Dutton, A. A., et al. 2016, MNRAS, 456, 3542, doi: 10.1093/mnras/stv2856

Tolstoy, E., Irwin, M. J., Helmi, A., et al. 2004, ApJL, 617, L119, doi: 10.1086/427388

Walker, M. G., Caldwell, N., Mateo, M., et al. 2023, ApJS, 268, 19, doi: 10.3847/1538-4365/acdd79

Walker, M. G., Mateo, M., Olszewski, E. W., et al. 2006, AJ, 131, 2114, doi: 10.1086/500193

Walker, M. G., & Peñarrubia, J. 2011, ApJ, 742, 20, doi: 10.1088/0004-637X/742/1/20

Wang, W., Han, J., Cooper, A. P., et al. 2015, MNRAS, 453, 377, doi: 10.1093/mnras/stv1647

Wang, W., White, S. D. M., Mandelbaum, R., et al. 2016, MNRAS, 456, 2301, doi: 10.1093/mnras/stv2809

Wang, W., Zhu, L., Li, Z., et al. 2022, ApJ, 941, 108, doi: 10.3847/1538-4357/ac9b19

Wang, W., Zhu, L., Jing, Y., et al. 2023, ApJ, 956, 91, doi: 10.3847/1538-4357/acf314

Watkins, L. L., van de Ven, G., den Brok, M., & van den Bosch, R. C. E. 2013, MNRAS, 436, 2598, doi: 10.1093/mnras/stt1756

Wolf, J., Martinez, G. D., Bullock, J. S., et al. 2010, MNRAS, 406, 1220, doi: 10.1111/j.1365-2966.2010.16753.x

Yang, X., Mo, H. J., Jing, Y. P., van den Bosch, F. C., & Chu, Y. 2004, MNRAS, 350, 1153, doi: 10.1111/j.1365-2966.2004.07744.x

Zhao, H. 1996, MNRAS, 278, 488, doi: 10.1093/mnras/278.2.488

Zhu, L., van de Ven, G., Watkins, L. L., & Posti, L. 2016a, MNRAS, 463, 1117, doi: 10.1093/mnras/stw2081

Zhu, L., Romanowsky, A. J., van de Ven, G., et al. 2016b, MNRAS, 462, 4001, doi: 10.1093/mnras/stw1931